Combustion and Flame 193 (2018) 397–416

Contents lists available at ScienceDirect

Combustion and Flame

journal homepage: www.elsevier.com/locate/combustflame

Including real fuel chemistry in LES of turbulent spray combustion

Anne Felden[a,*], Lucas Esclapez[a], Eleonore Riber[a], Bénédicte Cuenot[a], Hai Wang[b]

[a] CERFACS, CFD Team, 42 Av. Gaspard Coriolis, Toulouse 31057, France
[b] Department of Mechanical Engineering, Stanford University, Stanford, CA 94305, USA

ARTICLE INFO

Article history:
Received 15 November 2017
Revised 22 March 2018
Accepted 22 March 2018

Keywords:
Large Eddy Simulation
Spray combustion
Fuel effects
Gas turbines
Reduced chemistry

ABSTRACT

Large Eddy Simulation (LES) is progressively becoming a crucial design tool for the next generation of aeronautical combustion chambers. However, further improvements of the predictive capability of LES is required especially for predictions of pollutant formation. In general, the exact description of real fuel combustion requires to take into account thousands of unique chemical species involved in complex and highly non-linear chemical reaction mechanisms, and the direct integration of such chemistry in LES is not a viable path because of excessive computational demands and numerical stiffness. Modeling of real aeronautical transportation fuel is further complicated by the fact that kerosenes are complex blends of a large number of hydrocarbon compounds and their exact composition is very difficult to determine. In this work, we propose a new framework relying upon the Hybrid Chemistry (HyChem) approach and Analytically Reduced Chemistry (ARC) to allow a direct integration of real fuel chemistry in the compressible LES solver AVBP. The HyChem-ARC model is coupled with the Dynamically Thickened Flame LES model (DTFLES) and a Lagrangian description of the spray to investigate the turbulent two-phase flow flame in a lean direct injection combustor, fueled with Jet-A. The LES results are compared to experimental data in terms of gas velocity, temperature and species (CO_2, H_2O, CO, NO) mass fractions. It is found that the proposed methodology leads to very satisfying predictions of both the flow dynamics and the NO_x levels. Additionally, the refined level of chemistry description enables to gain valuable insights into flame/spray interactions as well as on the NO_x formation mechanism in such complex flame configurations. To improve further the results, a more detailed experimental characterization of the liquid fuel injection should be provided.

© 2018 The Combustion Institute. Published by Elsevier Inc. All rights reserved.

1. Introduction

Large Eddy Simulation (LES) is a widely used tool for the simulation of turbulent combustion in both academic and applied research [1]. At the heart of a combustion process, fuel pyrolysis and oxidation usually proceed through complex and highly non-linear reaction mechanisms that may involve thousands of unique chemical species. The direct integration of such detailed chemistry in LES is not a viable path, because of excessive computational demands and numerical stiffness [2]. The modeling and analysis of the strong coupling between turbulence and chemistry is also greatly complicated by involvement of many reaction pathways [3]. In spray combustion, finding a way to accommodate a realistic chemical description covering a wide range of operability is crucial. Increased variations of the length and time scales originate from the two phase nature of the flow [4], and as a result, a greater number of combustion regimes and flame structures may be observed than those in flames fueled by gaseous fuels [5,6]. In particular, partially-premixed combustion covers a wide range of equivalence ratio, as freshly evaporated, rich pockets mix while burning with the surrounding oxidant. Inhomogeneities in composition space may lead to non-negligible spatial and temporal variations of heat release rate, flame propagation rate or intermediate species mass fractions. The flammability limits could also broaden due to the stratification in temperature. All of these factors could impact the formation of pollutants.

In LES of complex geometries, chemical kinetics is often taken into account through globally fitted reaction schemes [7,8]. In such methods, 5 to 10 species interact in no more than one to four global reactions, the rate parameters of which are optimized against global flame properties over a specified range of conditions. Examples of LES using global schemes are numerous, in both gaseous [9–11], and spray configurations [12–14]. The use of these global reaction mechanisms represents a very crude approximation, often resulting in a narrow range of applicability (usually, under fuel-lean conditions), unless special treatments such as pressure and/or equivalence ratio dependent reaction rates are

* Corresponding author.
E-mail addresses: felden@cerfacs.fr, anne.felden@cerfacs.fr (A. Felden).

https://doi.org/10.1016/j.combustflame.2018.03.027
0010-2180/© 2018 The Combustion Institute. Published by Elsevier Inc. All rights reserved.

used [15]. With this approach, a physical description of the pollutant chemistry is impossible because the necessary intermediate species are not considered. Another classical approach to including realistic chemistry uses pre-tabulated laminar flame solutions based on detailed chemistry. This method assumes that thermo-chemical evolutions in the composition/temperature space can be parametrized by a reduced set of variables [16]. Techniques that fall into this category include the flame-generated manifold (FGM) [17], the Flame Prolongation of ILDM (FPI) [18] or the Flamelet Progress Variable (FPV) [19], all of which have been used with various turbulence-chemistry interaction models to perform LES of complex geometries operating under gaseous conditions [11,20]. For spray combustion, however, the use of these methods is complicated by the non-monotonicity of the mixture fraction due to the evaporation process and the intrinsic modification of the flame structure due to the spray [21]. Several methods have been proposed to address this issue. The simplest approach uses single-phase tabulated flamelets with adjusted fuel-side temperature to account for evaporation [22], while neglecting the interaction of the spray with the reaction zone. To account for the partially premixed gaseous flame structures, several authors proposed to employ hybrid premixed/partially-premixed/diffusion tabulated single-phase flamelets [23,24]. More advanced methods rely on tabulated laminar two-phase flamelets [25,26] to explicitly account for the spray/chemistry interactions in the LES [27]; but the methods require to increase the dimensionality of the look-up table. This dimensionality increase is also necessary in order to take into account complex phenomena such as thermal radiation and/or slow pollutant chemistry [28,29], making the use of tabulation not straightforward in complex flame structures.

Continued growth in computational power now enables to employ more detailed chemistry descriptions in LES. Analytically Reduced Chemistry (ARC) is a viable tool to bringing detailed chemistry in complex simulations (e.g. [30]). Such schemes, of about 10 to 30 transported species, are non-stiff by construction and can accurately describe combustion phenomena by retaining the most important species and reactions in a physically-justifiable way. Their use in LES of realistic 3D configurations is still recent. Work thus far has focused mainly on simple, single-component fuels such as methane [31–33]. ARC in two-phase, complex flow configurations remains limited in the literature. To our knowledge, only a handful of such studies are available, employing single-component fuels such as n-dodecane [34] or ethanol [35].

Adding to the aforementioned complexity of chemistry modeling in CFD, transportation fuels are in fact complex blends of a large number of hydrocarbons. Average fuel properties are known at the best, and large variations can be observed in the chemical composition from different fuel batches [36]. Fuel chemical property modeling is traditionally achieved through the use of fuel *surrogates*, consisting of several representative hydrocarbons. It is thought that if the main chemical classes of representative constituents are accounted for, all important properties of the fuel should be retrieved. Ideally, both physical (density, molecular weight, H/C ratio, viscosity, distillation curve) and chemical (ignition delay, flame speed, sooting tendency) properties should be matched by a comprehensive surrogate description [37]. However, this is an impractical proposition, as the number of surrogate components must be fairly large in order for the surrogate mixture to mimic accurately all or at least most of the properties just mentioned. In Wood et al. [38], a surrogate made up of a blend of 14 hydrocarbons was derived to reproduce the distillation and compositional characteristics of a JP-4, yet it is unclear whether the number of components is large enough to capture both the evaporation rate and fuel ignition properties. Violi et al. [39] developed several surrogates with 5 or more constituents to represent JP-8, targeting volatility (distillation curve) and sooting tendencies. Many other attempts at employing different targets for surrogate formulation, resulting in various proposed mixtures, are reported in the reviews by Dagaut and Cathonnet [40] or more recently, by Pitz and Mueller [41].

Considering such an exhaustive list of constituents is not a viable option for CFD implementation. With this intent in mind, recent work limits the number of components to four at the most. Dooley et al. [42], for example, proposed an experimental methodology for surrogate formulation by matching the radical pool of a real fuel along with four property targets (molecular weight, Threshold Sooting Index, H/C, Derived Cetane Number). They applied the method to a type of Jet-A (POSF 4658) fuel and derived three and four components surrogates followed by tests against a wide range of combustion data. Narayanaswamy et al. [43] developed an automated optimization tool to derive surrogates for average Jet-A/JP-8. A similar tool, with a different set of targets has also been proposed by Kim et al. [44] and later by Ahmed et al. [45] for ground transportation fuels. In most numerical studies employing these surrogates, reaction mechanisms are compiled from those of each component. However, the interaction of various pathways associated with each fuel component can become problematic when trying to reduce the size of the mechanism to make it affordable for turbulent simulations.

This paper presents an alternative approach to real fuel chemistry modeling in LES. This method combines the Hybrid Chemistry (HyChem) model recently introduced [46,47] with the ARC approach in a dynamic thickened flame framework (DTFLES [48]) in order to allow for an explicit integration of chemistry in LES. The first Section presents the HyChem methodology briefly, and provides details about the ARC derivation and validations. The experimental apparatus of the target configuration is presented in Section 3, while the numerical setup is detailed in Section 4. Reacting and non-reacting flow-field validations are presented in the first part of Section 5, before the results obtained for the turbulent spray flame are presented and assessed against experimental data in a second part.

2. Derivation of an ARC for Jet-A with NO_x chemistry

2.1. Jet-A POSF10325 specifications

In what follows, a specific Jet-A fuel is considered: the Jet-A POSF10325, which was procured from the Shell Mobile refinery in June 2013 in the context of the National Jet Fuel Combustion Program [49]. This batch is expected to be an average Jet-A fuel. Its properties are summarized in Table 1.

2.2. Derivation of the reaction model

As previously mentioned, the classical approach to modeling the combustion chemistry of this specific Jet-A fuel is based on the surrogate method. A recent work by Edwards [50] reports the derivation of two surrogates, both comprised of three hydrocarbons representative of the main hydrocarbon classes found in the fuel: a n-alkane, an *iso*-alkane and an aromatic. They were constructed to match the H/C ratio, smoke point, and DCN. However, reducing the resulting kinetic mechanisms did not lead to a viable scheme for LES. In the present investigation an alternative approach is selected and detailed in what follows.

2.2.1. The HyChem model

HyChem is a recently proposed, alternative modeling approach to the classical surrogate fuel method [46,47]. The method and the resulting reaction model are discussed briefly here; the reader is referred to the aforementioned publications for details. The approach relies on the assumption that any fuel, no matter

Table 1
Properties of the Jet-A (POSF10325).

Molecular formula	Composition (mass fraction [%])					Mol. Weight
	Aromatics	*iso*-Paraffins	*n*-Paraffins	Cycloparaffins	Alkenes	[kg/mol]
$C_{11.4}H_{22.1}$	18.66	29.45	20.03	31.86	< 0.001	156.0

H/C	Δh_c [MJ/kg]	DCN	T_{10} [K]	$T_{90} - T_{10}$ [K]	μ_l(300 K) [mPa s]	ρ_l(300 K) [kg/m^3]
1.91	43.1	48.3	450.0	67.8	1.37	794

how complex it is, would first decomposes into a handful of small molecules, and that it is the distribution of these pyrolysis products that would primarily impact the subsequent radical buildup and heat release rate. The pyrolysis products pool is dominated by hydrogen (H_2), methane (CH_4), ethylene (C_2H_4), propene (C_3H_6), *iso*-butene (i-C_4H_8), 1-butene (1-C_4H_8), benzene (C_6H_6) and toluene (C_7H_8). It follows that the combustion process can be decomposed into a fuel pyrolysis step and a subsequent oxidation process of the pyrolysis products. Detailed kinetic models for particular real fuels can thus be obtained by merging a pyrolysis mechanism comprised of a few lumped reactions, yielding the composition of the primary pyrolysis products, and a detailed foundational kinetic mechanism. The "fuel", in that case, is a mono-component lumped species. Its pyrolysis kinetic rates and products are determined from shock tube and flow reactor pyrolysis experiments, as well as from oxidative pyrolysis studies. It has been demonstrated that HyChem models capture shock-tube ignition delay times, laminar flame speeds and non-premixed flame extinction rates [47] over a wide range of pressure, temperature and equivalence ratio for at least a dozen jet, rocket and gasoline fuels. Examples for the jet and rocket fuels can be found in Xu et al. [47].

For the Jet-A (POSF10325) under consideration, the fuel breakdown is described by 6 lumped reactions, and ethylene constitutes the bulk of the pyrolysis products (the pyrolysis model is provided in Appendix B). Similarly to what was prescribed by Xu et al. [47], the detailed mechanism for the oxidation of the pyrolysis products is chosen to be the USC Mech II [51] for the high-temperature oxidation of C_{1-4} species, benzene and toluene. The USC Mech II is comprised of 111 species and 784 reversible reactions.

2.2.2. NO_x chemistry

A NO_x reaction sub-model is often added as a complementary set to hydrocarbon oxidation mechanisms. Note, however, that the levels of NO_x rely heavily upon the concentration of flame radicals such as O, OH and CH [52]. In that regard, because of the different assumptions made about the reaction rates, we expect different kinetic schemes to yield different levels of radicals even for the same fuel, which will eventually translates into very different NO levels.

For the current work, we chose the NO_x sub-mechanism of Luche [53], which is comprised of 17 species and 71 reactions. This NO_x sub-model was developed for the oxidation of a kerosene surrogate.

2.2.3. JetA_USCII_NOx detailed mechanism

The complete detailed mechanism, referred to as JetA_USCII_NOx in what follows, is comprised of a total of 129 species and 861 reactions. A schematic of the different sub-schemes of the JetA_USCII_NOx is provided in Fig. 1.

2.3. Derivation of the ARC

Solving for this mechanism directly is currently not feasible in LES. In this work, an ARC is derived following three automated steps.

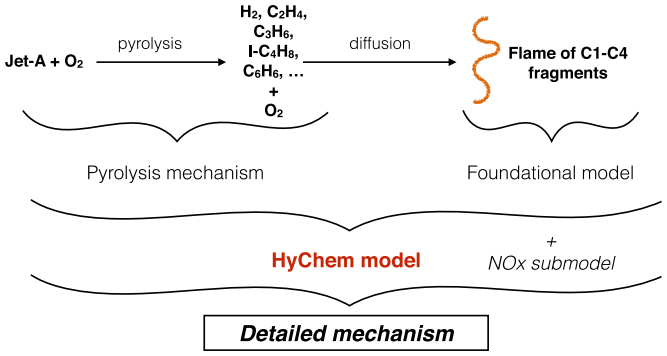

Fig. 1. Construction of the JetA_USCII_NOx detailed mechanism.

First, targets associated with a set of canonical zero- or one-dimensional configurations is prescribed, so that the reduction can be steered towards preserving predictive accuracy of those targets. Here the target types include one-dimensional laminar premixed flames (PF) and zero-dimensional auto-ignition computations (AI) under atmospheric pressure, representative of the flame configuration of Cai et al. [54]. The range of equivalence ratio (ϕ) extends from 0.8 to 1.3. Targets consist of auto-ignition time (τ_{ig}), burnt gas temperature T_b, laminar flame speed s_l, main species final values, and specific intermediate species profiles. The full set of targets is reported in Table 2.

Following the terminology from Turanyi [55], a skeletal reduction is performed first: unimportant species and reactions are removed from the detailed mechanism using the Directed Relation Graph with Error Propagation method (DRGEP) [56]. The resulting skeletal mechanism is comprised of 46 species and 547 reactions written explicitly in the forward or reverse directions. Assumptions about species characteristic timescales are then formulated, using the same reduction targets, in order to reduce the stiffness: 17 species are identified as being "quasi steady-state" species by the Level of Importance (LOI) criterion [57].

The resulting ARC, labelled ARC_29_JetANOx in what follows, retains 29 transported species and 17 QSS species. The retained species are listed in Fig. 2, along with an estimation of associated chemical time scales, evaluated from the diagonal of the Jacobian matrix obtained in a stoichiometric PF (black bars). The entire reduction was performed with the automated tool *YARC* developed by Pepiot [58].

The reduced mechanism allows for a direct implementation in the LES solver AVBP, with simplified transport data, as will be described in Section 4.1.

2.4. Validation

The performances of the ARC_29_JetANOx are evaluated against that of the detailed mechanism JetA_USCII_NOx in zero- and one-dimensional canonical test cases. Computations were performed with CANTERA [59] and FlameMaster [60]. The detailed mechanism is coupled to a complex transport formulation while for ARC, a

Table 2
List and specifications of the chemistry reduction.

Canonical test cases	Targeted range	Targeted constraints
PF	P = 1 atm - 300 K - ϕ = [0.8–1.3]	CO CO_2 C_2H_4 OH HR NO
AI	P = 1 atm - T = [1300–1700] K - ϕ = [0.8–1.3]	CO CO_2 C_2H_4 OH HR NO

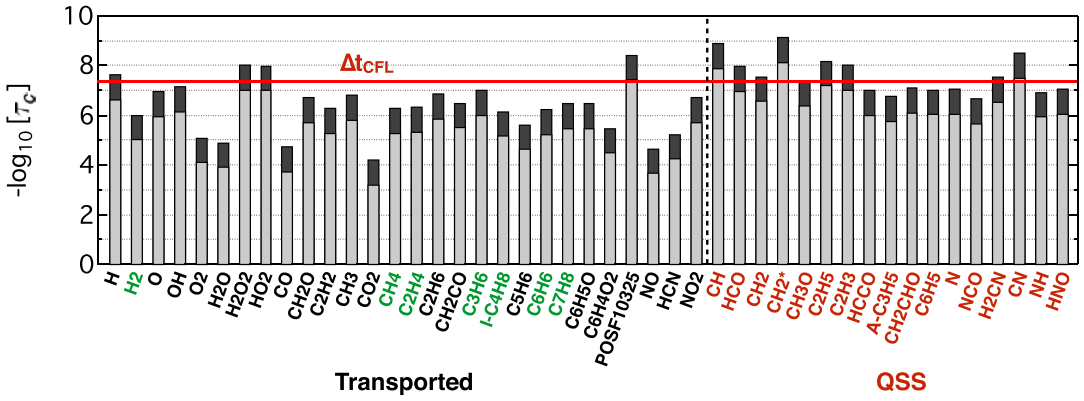

Fig. 2. Characteristic times of the transported and QSS species of the ARC_29_JetANOx. The difference between black and grey bars corresponds to the stiffness reduction induced by the DTFLES model, assuming a representative thickening factor of 10. $\Delta t_{CFL} = 5.10^{-8}$ s is the acoustic characteristic time scale of the target configuration. Green species represent the pyrolysis products from the HyChem model (Section 2.2.1). (For interpretation of the references to color in this figure legend, the reader is referred to the web version of this article.)

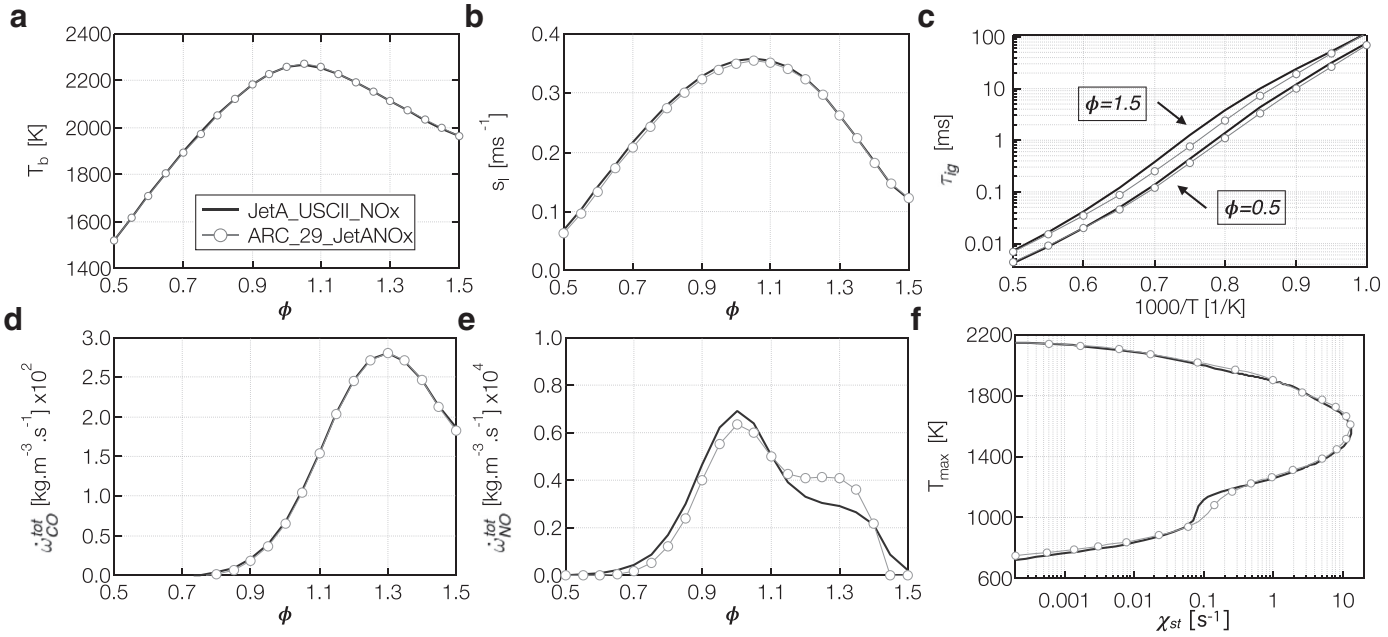

Fig. 3. Global performances of the ARC_29_JetANOx mechanism compared to the JetA_USCII_NOx detailed mechanism. PF test cases: (a) T_b, (b) s_l, (d) global CO production and (e) global NO production for T_i = 300 K, P = 1 bar. AI test cases: (c) τ_{ig} for ϕ = 0.5, 1.5, P = 1 bar. CF test cases: (f) $S-$curve for T_i = 300 K, P = 1 bar.

simplified transport model is employed, based on constant species Schmidt numbers and Prandtl number evaluated in the reaction zone of a representative complex transport PF. The same simplified transport model is used in LES (see Section 4.1).

PF and AI test cases are first considered. Global quantities targeted by the reduction procedure, such as the burnt gas temperature T_b, the flame speed s_l and the auto-ignition delay time τ_{ig} are shown to be accurately reproduced by the ARC_29_JetANOx, Fig. 3 (a)–(c). As expected from the physically-oriented reduction process, the range of validity of ARC_29_JetANOx extends well beyond the targeted condition range. Over the extended range displayed, the relative error in s_l is below 3%, except in very lean conditions where it can reach up to 8%. Predicted τ_{ig} are seen to be less accurate under rich conditions, but results are expected to be within experimental uncertainties. Pollutant production is assessed by computing the global CO/NO production, defined as:

$$\dot{\omega}^{tot}_{CO/NO} = \int_{c<0.98} \dot{\omega}_{CO/NO} dx \quad (1)$$

where the integration is limited to c = (Y_{CO} + Y_{CO_2}) < 0.98 to amplify the effects of chemical kinetics. Results are presented in Fig. 3 (d)–(e). An excellent agreement between the detailed mechanism and the ARC results is observed for CO global production, with a relative error computed over the entire range of equivalence ratio below 5%. NO global production is less accurately retrieved by the ARC mechanism, with errors ranging from 10 to 40% in rich conditions.

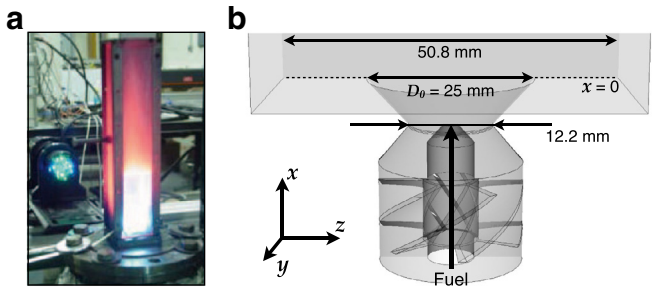

Fig. 4. (a) Picture of the experimental test rig [54]. (b) Details of the injection system.

Finally, *a-posteriori* tests on laminar strained counterflow diffusion flames configurations (CF) are performed. Indeed, because the target application is a two-phase flow burner, the occurrence of diffusion structures is expected. *S*−shaped curves of maximum temperature versus scalar dissipation rate at stoichiometry, χ_{st}, are plotted in Fig. 3(f) for both the JetA_USCII_NOx and the ARC_29_JetANOx. An overall good agreement is observed. In particular, the extinction scalar dissipation rate $\chi_{ext} = 10.5\ s^{-1}$ is perfectly matched by the ARC.

3. Target configuration

3.1. Experiment

The target configuration chosen in this work is the lean direct injection (LDI) combustor operated at NASA Glenn [54,61,62]. This choice was mainly driven by the use of a real aviation fuel, which is found only in a handful of lab-scale experiments [54,63,64], and by the wealth of experimental data available in terms of temperature and chemical species. This configuration therefore will allow an accurate validation of the proposed methodology to include realistic fuel chemistry in LES. A picture of the experimental facility is presented in Fig. 4(a) while details of the injection system are shown in Fig. 4(b). The burner consists of an axial swirler composed of six helicoidal vanes inclined at 60° and a PARKER pressure-swirl atomizer located in the center. The atomizer tip is located at the throat of a converging/diverging nozzle. The outer diameter of the nozzle at the combustion chamber dump plane is $D_0 = 0.025$ m. The combustion chamber has a height of 305 mm and a square section of length 50.8 mm. Quartz windows allow optical access from all sides.

The combustor is operated at ambient conditions ($P = 1$ atm, $T = 300$ K). Air is injected with a nominal mass flow rate of 8.16 g/s through a plenum upstream of the swirler vanes while liquid Jet-A fuel is injected through the atomizer with a mass flow rate of 0.415 g/s. These conditions correspond to a lean overall equivalence ratio ϕ_g of 0.75. Due to the low pressure in the fuel lines, the spray is found to exhibit unstable distribution patterns [54]. Laser Doppler Velocimetry was used to measure gas velocity while Phase Doppler Particle Analyzer measurements were performed for spray velocity and droplet size distribution [54]. Gas temperature and species profiles were obtained from thermocouple and isokinetic probes, respectively [62].

3.2. Previous studies

To the authors knowledge, the LDI combustor has been previously studied using LES by three groups [12,23,65]. All employed a Lagrangian approach to describe the liquid phase (although with different parameters), while the chemistry description and the flame turbulence-interaction model differed from one group to another. Patel and Menon [12] used the Linear Eddy Model (LEM) with a 3-steps global chemical scheme accounting for fuel oxidation as well as CO and NO formation, while the Jet-A was approximated by $C_{12}H_{23}$. El-Asrag et al. [65] employed the flamelet-progress variable (FPV) approach modified to account for radiation and NO formation [28], and the tabulated variables were calculated from steady counterflow diffusion flamelets obtained with the detailed mechanism of a two-components Jet-A surrogate [66]. Finally, a similar albeit multi-regime flamelet approach was followed by Knudsen and Pitsch [23].

While a good agreement with experimental data in terms of non-reacting gaseous velocity is reported in all studies, the spray statistics and time-averaged gaseous velocity was found to be in limited agreement with experiments. Patel and Menon [12] and Knudsen and Pitsch [23] highlighted the sensitivity of the LES predictive capabilities to the spray description by evaluating the effect of secondary break-up and spray boundary conditions, respectively. A complete comparison between LES and experiments in terms of temperature and species mass fractions is only reported in Knudsen and Pitsch [23], where the combustion products were found to be fairly well predicted, whereas CO predictions exhibited larger errors. The analysis provided in El-Asrag et al. [65] is limited to the effect of radiative heat losses on the temperature and NO fields, indicating that including radiative heat transfer might improve temperature and pollutant species predictions.

4. Computational approach

4.1. Governing equations

4.1.1. Gas phase equations

In this study, the spatially filtered compressible Navier–Stokes equations are considered, where $\bar{\cdot}$ and $\tilde{\cdot}$ represent Reynolds and Favre spatial filtering respectively. In the DTFLES framework (see Section 4.1.3) and assuming a dilute spray regime, the conservation equations write:

$$\frac{\partial \overline{\rho}}{\partial t} + \frac{\partial \overline{\rho}\widetilde{u}_j}{\partial x_j} = \frac{\overline{\Gamma}}{\mathcal{F}} \tag{2}$$

$$\frac{\partial \overline{\rho}\widetilde{u}_i}{\partial t} + \frac{\partial \overline{\rho}\widetilde{u}_i\widetilde{u}_j}{\partial x_j} = -\frac{\partial}{\partial x_j}\left[\overline{p}\delta_{ij} - \overline{\tau}_{ij} - \overline{\tau}_{ij}^{sgs}\right] + \widetilde{u}_{d,i}\frac{\overline{\Gamma}}{\mathcal{F}} + \frac{\overline{F}_{d,i}}{\mathcal{F}} \tag{3}$$

$$\frac{\partial \overline{\rho}\widetilde{E}}{\partial t} + \frac{\partial \overline{\rho}\widetilde{E}\widetilde{u}_j}{\partial x_j} = -\frac{\partial}{\partial x_j}\left[\overline{u_i(p\delta_{ij} - \tau_{ij})} + \mathcal{E}\mathcal{F}\overline{q}_j + (1-\mathcal{S})\overline{q}_j^{sgs}\right] + \frac{\mathcal{E}\overline{\dot{\omega}}_T}{\mathcal{F}} + \frac{\overline{\Pi}}{\mathcal{F}} + \frac{1}{2}\widetilde{u}_{d,i}^2\frac{\overline{\Gamma}}{\mathcal{F}} - \widetilde{u}_{p,i}\frac{\overline{F}_{d,i}}{\mathcal{F}} \tag{4}$$

$$\frac{\partial \overline{\rho}\widetilde{Y}_k}{\partial t} + \frac{\partial \overline{\rho}\widetilde{Y}_k\widetilde{u}_j}{\partial x_j} = -\frac{\partial}{\partial x_j}\left[\mathcal{E}\mathcal{F}\overline{J}_{k,j} + (1-\mathcal{S})\overline{J}_{k,j}^{sgs}\right] + \frac{\mathcal{E}\overline{\dot{\omega}}_k}{\mathcal{F}} + \frac{\overline{\Gamma}}{\mathcal{F}}\delta_{k,F} \quad \text{for } k = 1, N_s \tag{5}$$

where ρ is the gas density, u_j is the gas j*th* component of velocity, E is the total non-chemical energy, p is the static pressure, and Y_k is the mass fraction of species k. $\mathcal{F}$, $\mathcal{E}$ and $\mathcal{S}$ are the thickening factor, the efficiency function and the flame sensor, respectively, introduced by the thickened flame model (see Section 4.1.3). $\overline{\tau}_{ij}$ is the filtered stress tensor, $\overline{q}_j$ is the filtered heat diffusive flux and $\overline{J}_{k,j}$ is the filtered species diffusive flux evaluated with a simplified transport model. Indeed, in order to afford the direct implementation of reduced chemistries into the LES solver, transport properties are expressed in function of a constant adimensional Schmidt number (Sc_k) for each species k and a constant Prandtl (Pr) number. The diffusivity of each species k is thus evaluated as $D_k = \mu/(\rho Sc_k)$ while the thermal conductivity is expressed as $\lambda = \mu c_p/Pr$ where

μ is the dynamic viscosity and c_p is the constant pressure heat capacity. μ is evaluated from the mixture temperature following a Power law. The superscript *sgs* indicates sub-grid scale contributions arising from the LES filtering, described in Section 4.1.3. Finally, $\overline{\Gamma}$, $\overline{F}_{d,i}$ and $\overline{\Pi}$ are the liquid phase source terms, detailed in Section 4.1.2.

Note that neither radiation modeling nor wall hear losses are included in the present simulations.

4.1.2. Dispersed phase description

The spray is described with a Lagrangian approach where the droplet motion is described by the Basset–Boussinesq–Oseen equations [67]. Under the assumption of small droplet diameter (d_p) compared to the grid size, small droplet Reynolds number (Re_p) and large density ratio between the liquid and the gas, the droplet motion equations write:

$$\frac{d\boldsymbol{x}_p}{dt} = \boldsymbol{u}_p \tag{6}$$

$$\frac{d\boldsymbol{u}_p}{dt} = \frac{1}{\tau_p}(\boldsymbol{u}_{@p} - \boldsymbol{u}_p) = \frac{\boldsymbol{F}_d}{m_p} \tag{7}$$

where $\boldsymbol{x}_p$ is the droplet position vector and $\boldsymbol{u}_p$ is the droplet velocity vector, $\boldsymbol{u}_{@p}$ is the gaseous velocity vector at the droplet position and m_p is the droplet mass. τ_p is the droplet relaxation time, estimated as the Stokes characteristic time:

$$\tau_d = \frac{4}{3}\frac{\rho_l}{\rho}\frac{d_p}{C_D|\boldsymbol{u}_{@p} - \boldsymbol{u}_p|} \tag{8}$$

where ρ_l is the liquid density. C_D is the drag coefficient given in terms of the droplet Reynolds number by the Schiller and Naumann correlation [68]:

$$C_D = \frac{24}{\mathrm{Re}_p}(1 + 0.15\mathrm{Re}_p^{0.687}) \tag{9}$$

$$\mathrm{Re}_p = \frac{|\boldsymbol{u}_{@p} - \boldsymbol{u}_p|d_p}{\nu} \tag{10}$$

Under the assumption of dilute spray regime, individual droplet evaporation is considered, where droplet interactions are neglected. The temporal evolution of the droplet mass and temperature are given by:

$$\dot{m}_p = \frac{dm_p}{dt} = -\pi d_p \frac{\mathrm{Sh}}{Sc_F}\mu \ln(1 + B_M) \tag{11}$$

$$\begin{aligned}\frac{dT_d}{dt} &= \frac{1}{c_{p,L}m_p}\left(-\phi_g + \dot{m}_p L_{h,F}\right) \\ &= \frac{1}{c_{p,L}m_p}\left(\pi d_p \mu c_p \frac{\mathrm{Nu}}{Pr}(T_{g@p} - T_p)\frac{\ln(1+B_T)}{B_T} + \dot{m}_p L_{h,F}\right)\end{aligned} \tag{12}$$

where T_p is the droplet temperature, $T_{g@p}$ is the gas temperature interpolated at the droplet position, $c_{p,\,L}$ is the liquid heat capacity and $L_{h,\,F}$ is the latent heat of evaporation of liquid fuel. Sh and Nu are the Sherwood number and Nusselt number, respectively, evaluated using the Ranz–Marshall empirical correlations [69]. μ and c_p are here estimated with the classical '1/3 rule' between far field and droplet surface conditions [70]. Finally, B_M and B_T are the mass and temperature Spalding numbers evaluated iteratively following the Abramzon–Sirignano model [71].

The Lagrangian source terms appearing in the Navier–Stokes equations are finally computed using:

$$\overline{\Gamma} = \frac{1}{\Delta V}\sum_{d\in\Delta V}\Psi(\boldsymbol{x}_d)\dot{m}_d \tag{13}$$

$$\overline{\boldsymbol{F}_d} = \frac{1}{\Delta V}\sum_{d\in\Delta V}\Psi(\boldsymbol{x}_d)\boldsymbol{F}_d \tag{14}$$

$$\overline{\Pi} = \frac{1}{\Delta V}\sum_{d\in\Delta V}\Psi(\boldsymbol{x}_d)(\phi_g + \dot{m}_d h_{v,F}(T_d)) \tag{15}$$

where ΔV is the local control volume in which the droplet is located (usually the cell) and $\Psi(\boldsymbol{x}_d)$ an inverse distance distribution function between the particles position nodes associated with the local control volume.

4.1.3. LES sub-grid scale closures

In the present study, the SIGMA eddy-dissipation model [72] is used to evaluate the sub-grid scale Reynold stress tensor τ_{ij}^{sgs}. Heat and species sgs transport are modeled with a gradient assumption relying on a constant turbulent Prandtl and constant turbulent Schmidt number, respectively ($\mathrm{Pr}_t = \mathrm{Sc}_t = 0.6$).

The DTFLES model of Colin et al. [48] is employed to account for turbulence/chemistry interactions. This approach can be seen as a modification of time ($t \rightarrow \mathcal{F}t$) and space ($\boldsymbol{x} \rightarrow \mathcal{F}\boldsymbol{x}$), enabling to virtually thicken the flame front (by a factor $\mathcal{F}$) to allow a direct resolution of the chemistry on the LES grid. As a consequence, and for consistency, the same scale transform must be applied to the liquid phase (see the Navier–Stokes equations presented in Section 4.1.1) [73]. Since about 5 grid points in the flame thickness is usually considered sufficient for a proper resolution, an evaluation of a local thickening factor can be defined as:

$$\mathcal{F} = 5\frac{\Delta x}{\delta_l^0} \tag{16}$$

based on a theoretical flame thickness δ_l^0 and on the local mesh size Δx. This evaluation is further refined through the use of a dynamic sensor $\mathcal{S}$, detecting regions of high heat release rate, in order to only apply the thickening factor where it is necessary. The final thickening factor then writes $\mathcal{F}^* = 1 + (\mathcal{F} - 1)\mathcal{S}$. In the present study, $\mathcal{S}$ is constructed by comparing local values of heat release rate to those expected under the same operating conditions in a laminar premixed flame. Note that in a thickened flame, a reduction of the chemical temporal stiffness is observed, as illustrated in Fig. 2 showing the effect of a thickening factor of order 10 on the chemical time scale of each species. To account for the loss of flame surface induced by the flame thickening, an efficiency function $\mathcal{E}$ is introduced to provide an estimate of the sub-grid flame surface wrinkling. The efficiency function formulation of Charlette et al. [74] is used in this work. Note, finally, that all laminar unstrained flame characteristics appearing in this model (δ_l^0 and s_l^0) are tabulated in function of the equivalence ratio in order to optimize the model effect to the local flow conditions.

No sgs model is employed to evaluate the gas properties at the droplet position [75] in the present study.

4.2. Numerical set-up

The computational domain comprises the entire combustion chamber and the injection system up to the annular plenum upstream of the swirler. The computational domain, displayed in Fig. 5 (a), is fully discretized using tetrahedra with size varying from 0.25 mm close to the injection system to about 3 mm in the downstream part of the combustion chamber. The final computational domain contains over 4 millions nodes and 23 millions tetrahedra. Figure 5 (b) displays a close-up of the mesh of the near injection.

Simulations are performed with the compressible, massively-parallel LES solver AVBP [76]. It uses an explicit time-stepping with a third order in time and space two-step Taylor–Galerkin finite element scheme for the resolution of the convective fluxes [77] and a second order Galerkin scheme for the diffusive fluxes. Inlet and

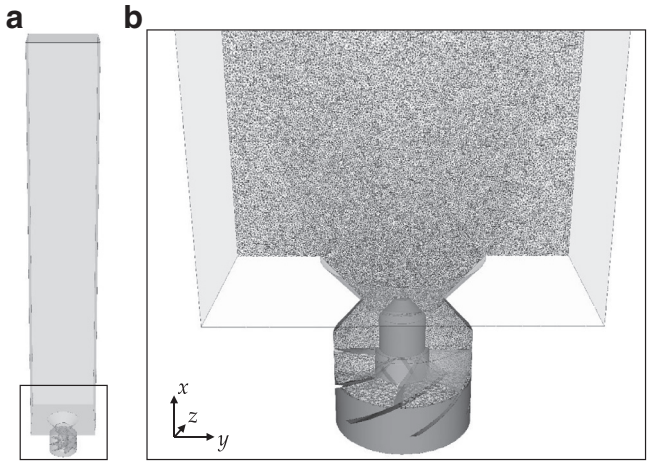

Fig. 5. a) Entire computational domain and b) Mesh resolution at the vicinity of the injection system.

outlet boundary conditions are prescribed using the NSCBC approach [78] while walls are considered adiabatic and non-slipping.

Lagrangian particles are advanced in time with a semi-implicit Euler scheme. The interpolation of gas properties to the particle location is performed using a first order Taylor reconstruction from the closest point. A poly-disperse spray injection boundary condition is prescribed at the pressure-swirl nozzle using the FIM-UR methodology described in [79]. Drops are injected with a temperature of 300 K. Based on the work of Knudsen and Pitsch [23], a spray angle of 61° with a log-normal diameter distribution is employed in this work, parametrized with a mean of 17 μm and a standard deviation of 20 μm. No secondary break-up model was employed.

An analysis of the droplet/wall interactions along the chamber walls leads to a wide range of impact energy C_{spl}, defined as C_{spl} =We.Oh$^{-2/5}$, where We is the impact Weber number We=$\rho_l 2r_d|\boldsymbol{u}_d \cdot \boldsymbol{n}|/\sigma_l$ and Oh is the Ohnesorge number Oh=$\mu_l/\sqrt{\rho_l\sigma_l 2r_d}$. In these expressions, σ_l is the liquid surface tension, μ_l is the liquid viscosity and $\boldsymbol{n}$ is the wall normal vector. Therefore, a splashing model is used in this work [80], in which droplets either stick to the wall or are partly splashed away, depending upon a critical impact energy $C_{spl,\,crit}$ and a characteristic temperature T_N (Nukiyama temperature). In this model, the splashed droplet size distribution follows a Rosin-Rammler function, and their velocity primarily depends upon the energy of impact.

5. Time-averaged LES results

5.1. Non-reacting flow validation

For validation purposes, the time-averaged non-reacting gas velocity fields are compared to experiments. Note that no liquid is injected in either the experiment nor the simulation in the non-reacting case. LES data are collected over 92 ms, corresponding to 12 flow-through times in the combustor. Profiles are extracted at four axial positions downstream of the injector tip, marked in Fig. 7 (b), and are presented in Fig. 6. Overall, LES results are in very good agreement with measurements in terms of inner recirculation zone (IRZ) width and velocity magnitude, as well as turbulent velocity fluctuations levels. However, we observe some discrepancies on the first profile ($x = 5$ mm), which might be due to the presence of wake effects from the swirler blades. Indeed the orientation of the swirler with respect to the measurement plane was not provided. Note the large opening angle of the swirled jet, which is characteristic of high swirl numbers. Here, the swirl number measured at $x = 0.0$ mm is 1.0, substantially larger than the critical swirl number of 0.6. The shear layer between the IRZ and the incoming swirled flow exhibits large fluctuations associated with a precessing vortex core (PVC), visible on the turbulent velocity profile at $x = 5$ mm of Fig. 6. The frequency of this PVC is estimated to be ≈4 kHz.

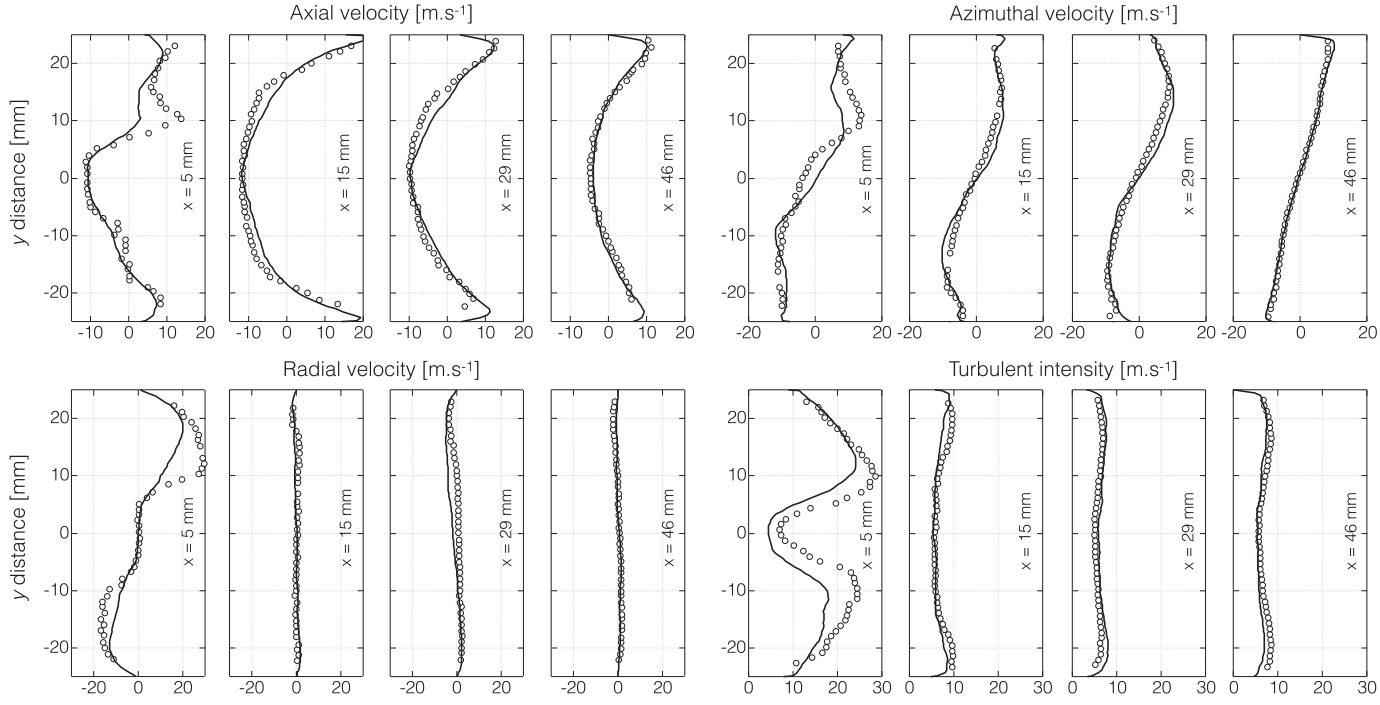

Fig. 6. Profiles of time-averaged gas velocity components and turbulent intensity at $x = 5$ mm, 15 mm, 29 mm and 46 mm in non-reacting conditions. Symbols: experiments, black line: LES.

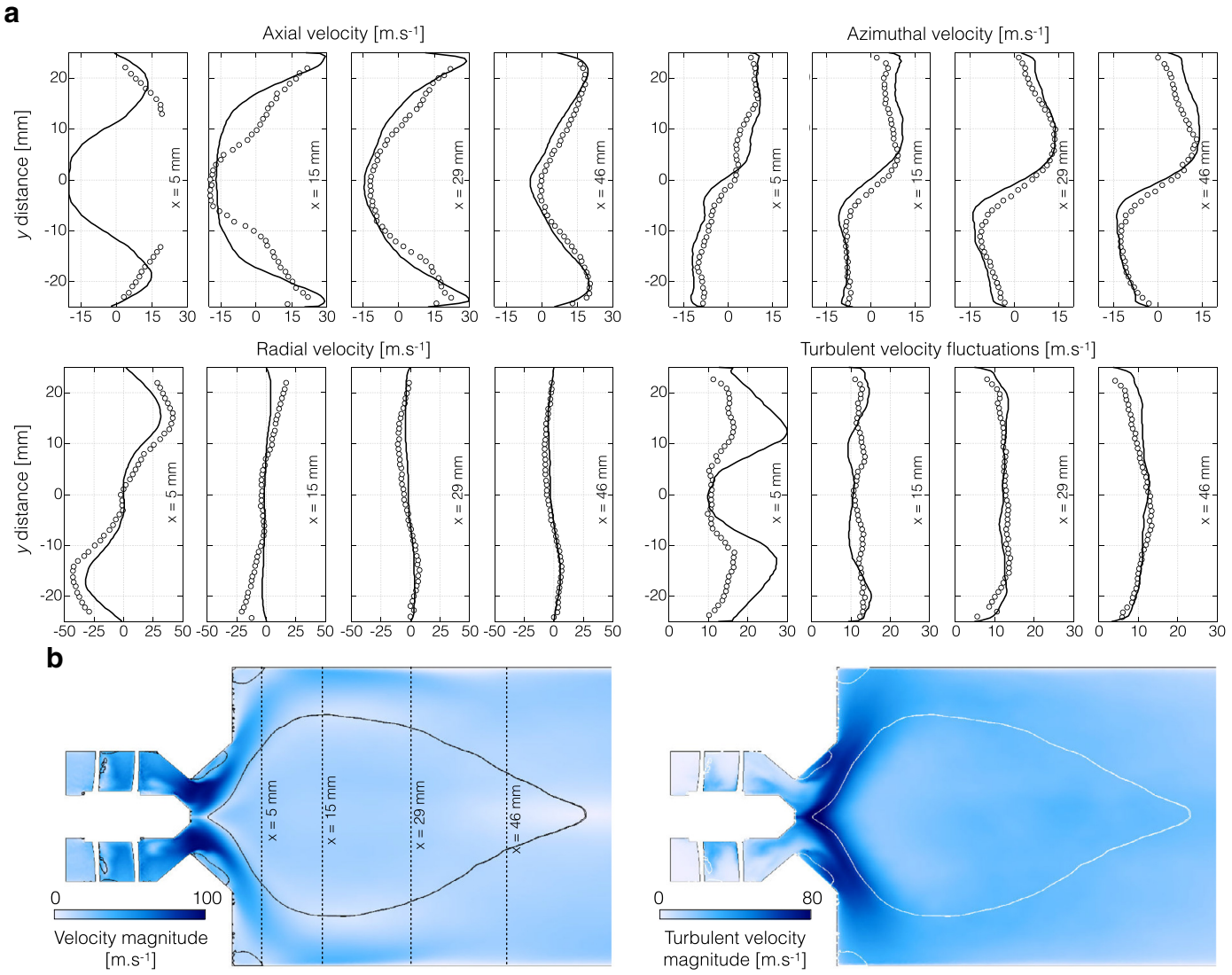

Fig. 7. (a) Profiles of time-averaged mean velocity and turbulent intensity at $x = 5$ mm, 15 mm, 29 mm and 46 mm in reacting conditions. Symbols: experiments, black line: LES. (b) Time-averaged fields of velocity magnitude and turbulent velocity magnitude in a z-normal central cut plane from the LES. The iso-contour indicates the position of the zero axial velocity.

5.2. Reacting flow validation

LES statistics presented in this Section were collected over 100 ms, corresponding to about 13 flow-through times of the combustor.

5.2.1. Gaseous flow

The main flow structures in the reacting case are similar to those of the non-reacting case. Figure 7(b) shows time-averaged velocity magnitude and turbulent velocity magnitude contours in a z-normal central plane, along with the zero axial velocity iso-contours, while a quantitative comparison between LES and experiments is provided in Fig. 7(a). The IRZ is found to be narrower and shorter than in the non-reacting case, extending from just downstream of the pressure-swirl nozzle to about $x = 2\ D_0$ (i.e., 50 mm). The negative axial velocity near the injection is also found to be significantly larger in the reacting case, indicating that the recirculation, playing an important role in the flame stabilization mechanism, is also impacted by the flame. The iso-contours of zero axial velocity highlights small outer recirculation zones in the corners of the combustion chamber as well as a small recirculation in the divergent section of the injection system. LES predictions are found to match well the experimental data, except at the vicinity of the injector where the width of the IRZ and the turbulent intensity are overestimated. Similar differences were also reported in previous numerical studies [23] and can at least partially be attributed to the position of the flame which, as will be discussed below, is found to sit closer to the injection system in the LES than in the experiments. Note also that in the shear layer at the boundary of the IRZ (see Fig. 8(a)), the spray exhibit a large density, strongly suggesting experimental uncertainties, and finally that the same reason than in the non-reacting case can also be invoked regarding the orientation of the measurement plane.

5.2.2. Spray

Figure 8(a) shows a comparison of LES spray statistics with experimental data and Fig. 8(b) shows the mean liquid volume fraction field in the central z-normal plane, constructed by projection of Lagrangian datasets. LES data are collected from 130 instantaneous Lagrangian solutions. Note that to ensure a statistical convergence, the data presented in Fig. 8(a) are azimuthally averaged so that only half of the profiles are showed (starting at $y = 0$). Radial

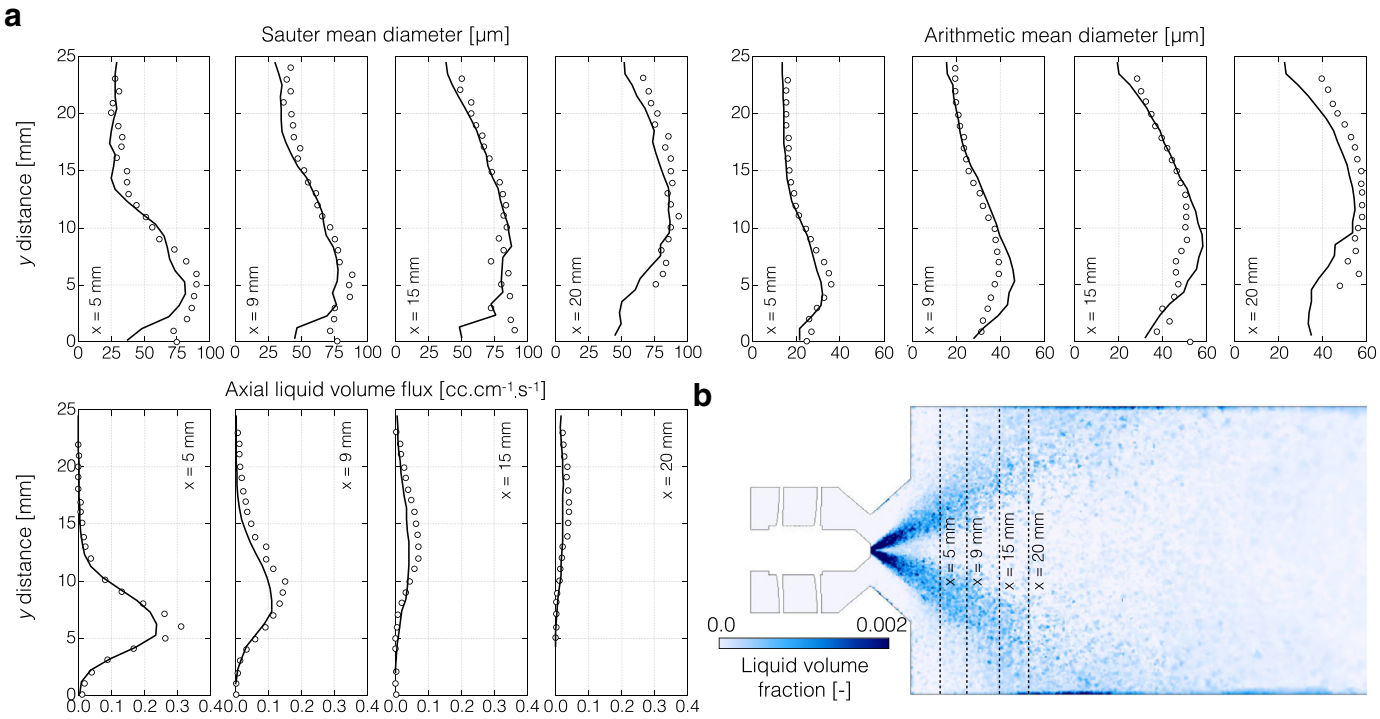

Fig. 8. (a) Profiles of time-averaged Sauter Mean Diameter (SMD), arithmetic mean diameter (D10) and axial liquid volume flux at $x = 5$ mm, 15 mm, 29 mm and 46 mm in reacting conditions. Symbols: experiments, black line: LES. (b) Time-averaged fields of liquid volume fraction in a z-normal central cut plane.

profiles of sauter mean diameter (SMD) and mean diameter (D10) are presented first. The agreement between LES and experiment is very good at all the measured positions, with only a noticeable under-prediction of the SMD along the injector axis and of the D10 at 20 mm. The very reasonable agreement on the first profile validates the spray boundary conditions. Note the differences between the SMD and the D10 close to injector, suggesting a wide dispersion of the droplet size distribution in this zone. This is especially true close to the injector axis, where large droplets are able to penetrate the IRZ while small droplets are deflected. At increasing distance from the injector, both the SMD and the D10 increase while getting closer, indicating that small droplets are progressively vaporized and that the local droplet size distribution gets narrower. This effect is well predicted in the LES, validating the modeling approach for droplet dispersion and evaporation.

Finally, the axial liquid volume flux is computed and compared to experiment, demonstrating that the spray angle and velocity are also well reproduced. Note that the liquid flux is under-estimated by the LES, which is found to be due to a faster evaporation resulting from an upstream shift of the flame position compared to experiments. Figure 8(b) indicates that the spray density is rather high at the vicinity of the injector nozzle, but rapidly decreases downstream of the dump plane, validating the hypothesis of dilute spray. Finally, past 20 mm from the dump plane, high liquid volume fraction is found along the combustor walls as a result of the spray/wall interaction. It will be shown later that this affects the species distribution.

5.2.3. Temperature and species

Figure 9(a) compares experimental and numerical radial profiles of gaseous temperature and major species, at several axial locations identified by vertical solid lines in Fig. 9(b). H_2O and CO_2 evolutions are very well retrieved by the LES, even though with less asymmetry than in the experiment. Note that if some asymmetry is to be expected from the 6-vanes swirler, the LES results suggest non-negligible experimental uncertainties. The agreement on the temperature profiles is not as good, particularly for $x <$ 20 mm. The experimental bimodal shape seen at $x = 20$ mm, revealing the intermittent presence of a flame, is found by the LES further upstream, at $x = 10$ mm, suggesting a shift of the main flame front towards the injector. An inspection of the mean stoichiometric iso-contour, superimposed to the mean fields of temperature and major species mass fractions (Fig. 9(b)), confirms that the region of highest reactivity is preferably located upstream of the first profile location. Despite this shift, however, the two peaks on the CO profile at 20 mm, representative of the early post-flame region, are accurately predicted by the LES. It is noted that the main flame appears lifted in both LES and experiment, in correspondence with the mean position of the tip of the IRZ seen in Fig. 8(b).

Further downstream, there seems to be an accumulation of CO along the walls, accompanied by a decrease of temperature, in both LES and experiment. It is reminded that no heat losses are included in the simulation. This phenomenon is therefore attributed to the accumulation of droplets resulting from the jet impact on the walls (Fig. 8). This forms regions of very rich mixture fraction, as shown by the stoichiometric iso-contours along the walls, around $x = 40$ mm in Fig. 9(b). At $x = 60$ mm, the temperature is seen to be overpredicted near the centerline. A closer examination of the experimental data indicates that the temperature at the outlet of the combustor rig is below the theoretical adiabatic value at the overall ϕ_g, by approximately 300 K. This difference suggests heat losses (radiation, wall losses) and/or incomplete combustion.

NO data are presented in Fig. 10(a) and (b). LES results are compared to experiment at several axial positions, with the last one ($x = 150$ mm) at half of the combustion chamber length. NO levels are found to be highest in the core of the IRZ, in the vicinity of the main flame, and significantly smaller along the walls for $x < 60$ mm, coinciding with low temperature regions where the jet impacts. NO levels along the centerline are seen to slightly increase with increasing distance from the injector. Overall, the main trends and levels are found to be very well captured by the LES, validating

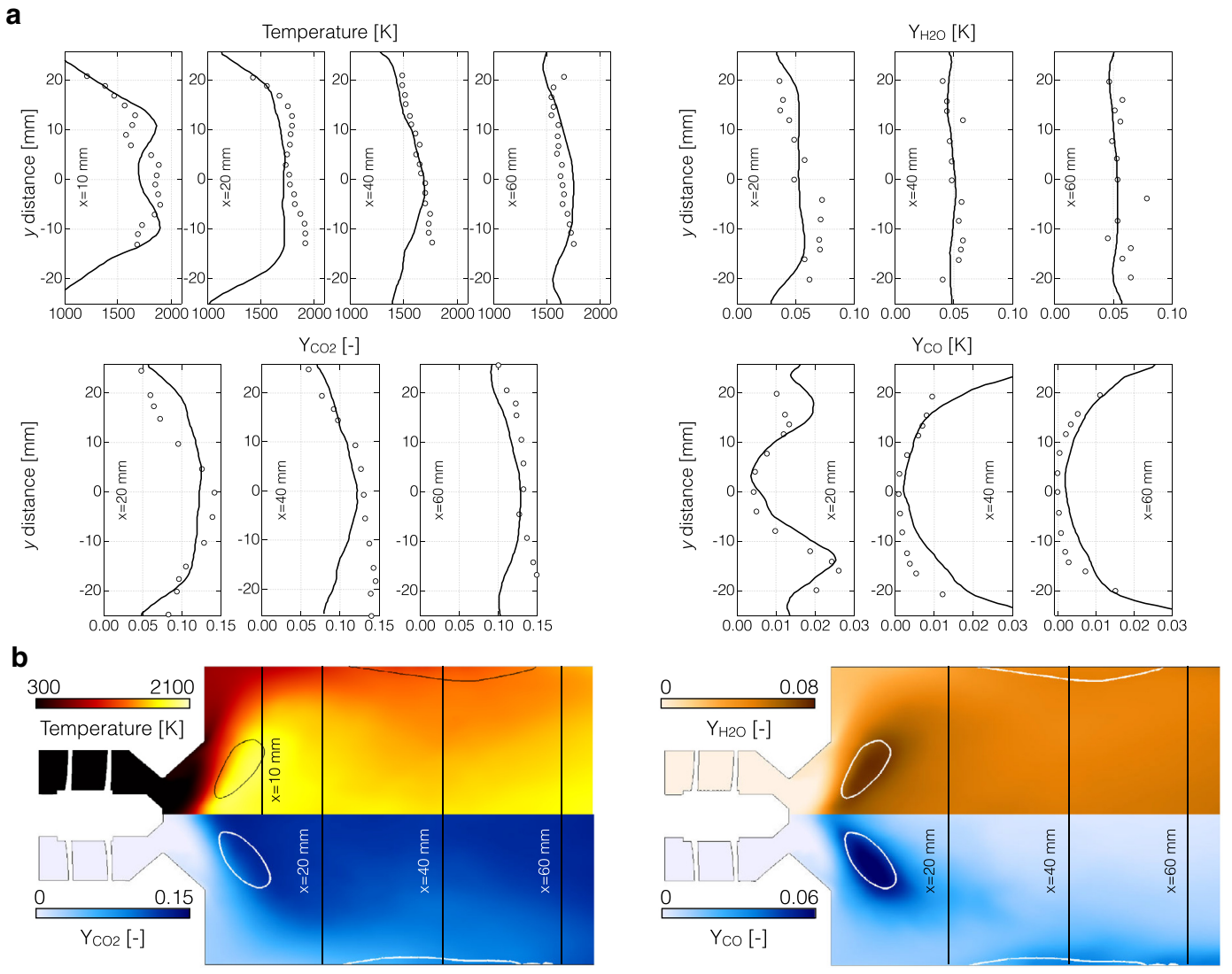

Fig. 9. (a) Profiles of time-averaged temperature and selected species (CO_2, H_2O and CO) at x = 20 mm, 40 mm and 60 mm in reacting conditions. Symbols: experiments, black line: LES. (b) Time-averaged fields of temperature and selected species (CO_2, H_2O and CO) in a z-normal central cut plane. The iso-contour indicates the position of the stoichiometric line.

a-posteriori the NO_x sub-mechanism. The shape of the first profile, at $x = 20$ mm, is the least well retrieved by the LES, with levels that are too high in the shear layer. This is consistent with a flame front shifted towards smaller axial positions, leading to post-flame levels already reached at $x = 20$ mm. Consistently with increasing temperature levels observed near the chamber walls, Fig. 9(a), NO levels are found to increase after $x = 60$ mm near the walls. No data are available for these radial positions, however.

6. Instantaneous flame structure

6.1. Spray flame analysis

6.1.1. Topology of the reacting particle laden flow

The instantaneous flame structure is depicted in Fig. 11 showing contours of temperature, heat release rate and several species mass fractions in a central z-normal cut plane. Iso-contours of stoichiometric mixture fraction $Y_z^{st} = 0.063$ are superimposed, where Y_z is defined following Bilger [81]. The spray is represented by grey spheres scaled by the droplet radius. The flame presents a complex structure, where three main combustion zones can be identified (Fig. 11(a)): (1) a first flame is located in the upstream part of the IRZ around a torus of rich burnt gases, (2) a second flame front extends downstream in between the IRZ and the ORZ, (3) individual burning droplets are spread throughout the recirculation zone. Figure 11(b) shows that the fuel mass fraction is negligible upstream and in the flame zone (1), but reaches values around 0.04 close to the walls in the downstream part of the flame zone (2). In contrast, pyrolysis products (listed in Section 2.2.1) and acetylene (C_2H_2), shown in Fig. 11(c), are present in significant proportions in the rich torus of burnt gases (zone (1), Fig. 11(d)), and in smaller proportions upstream of the reaction zone (2). This indicates that the fuel does not pre-vaporize upstream of the reaction zone (1), due to the too cold air and liquid temperature at injection. The fuel is massively vaporized in the core of the flame front (1), and the subsequent pyrolysis of the gaseous Jet-A is very fast because of the very high surrounding temperature. The fact that acetylene, which is not a direct pyrolysis product of the HyChem model, is present in such large proportions, is also a result of the high temperatures and overall rich mixtures prevailing in the torus, favoring the decomposition of ethylene into acetylene. In the downstream part of the reaction zone (2), the lower temperatures and overall lean conditions slow down the fuel pyrolysis and further decomposition of the pyrolysis products.

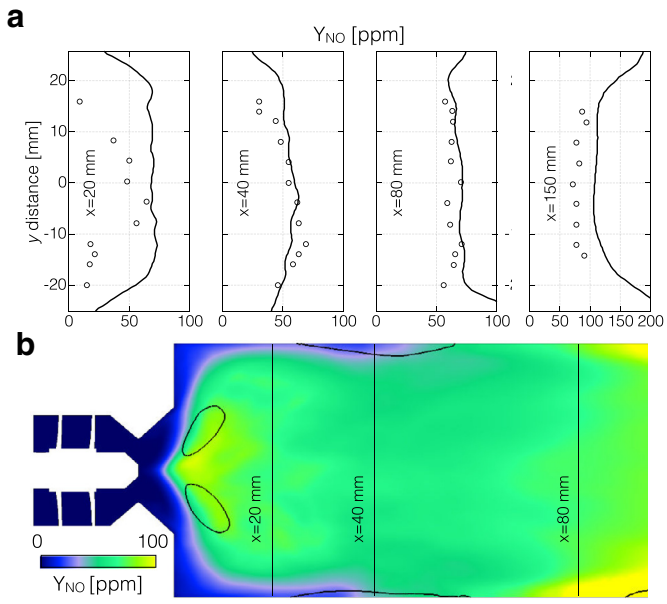

Fig. 10. (a) Profiles of time-averaged NO species at $x = 20$ mm, 40 mm, 80 mm and 150 mm in reacting conditions. Symbols: experiments, black line: LES. (b) Time-averaged fields of NO species in a z-normal central cut plane. The iso-contour indicates the position of the stoichiometric line.

The topology of these three combustion zones can be related to the spray dispersion and evaporation. Figure 12(a) displays the axial evolution of the evaporation rate, integrated over x-normal planes. Data are collected from 20 instantaneous solutions spanning 10 ms. Evaporation is found to peak around $x = 17$ mm, corresponding to the axial position of the rich torus of burnt gases, as well as to weak flame fronts (2). A plateau of evaporation is also seen in between $x = 25$ mm and $x = 50$ mm, suggesting that an important activity still takes place behind the main reaction front (1), albeit more spread out. The cumulative integrated evaporation rate normalized by the injection rate is also displayed as function of the axial position. It indicates that 40% of the fuel is evaporated before $x = 20$ mm and that more than half of the injected fuel evaporates in the flame fronts alongside the walls or as isolated droplets in the IRZ. Note also that almost all of the liquid fuel has evaporated by $x = 100$ mm. In an attempt to differentiate between the contribution of the reaction zone (1) and fronts (2) to the amplitude of the evaporation peak, Fig. 12(b) shows the integrated evaporation rate conditioned on the gas temperature. Two evaporation peaks are observed, around 950 K and 1800 K: the first one corresponds to intermediate temperature regions located in the ORZ, while the second one corresponds to the burned gas torus (1). Evaporation is highest in the latter region, thus confirmed as being the preferential location for evaporation.

The droplets dynamics in reaction front (1) is therefore critical for flame stabilization, and explains the strong dependency of LES predictions to inlet spray parameters [23]. Figure 13 displays scatterplots of droplets axial velocity against axial gaseous velocity, interpolated at the droplets position. Figure 13(a) is colored by the droplets size, while Fig. 13(b) is colored by the gaseous temperature. Most of the relatively small droplets ($d_p < 20$ μm), referred to as type (A) and framed in green in Fig. 13, fuel the upstream part of reaction zone (1). Their velocity is seen to rapidly equilibrate with that of the gas, as evidenced by their tendency to gather on a straight y = x line (grey dashed line in Fig. 13(a)). Their rapid evaporation is primarily responsible for the peak in evaporation rate (see Fig. 12(a)) and for the formation of the rich torus around which lies flame (1). Both figures indicate that larger droplets ($d_p > 40$ μm), referred to as type (B) and framed in black in Fig. 13, penetrate the IRZ. A non-negligible portion of these

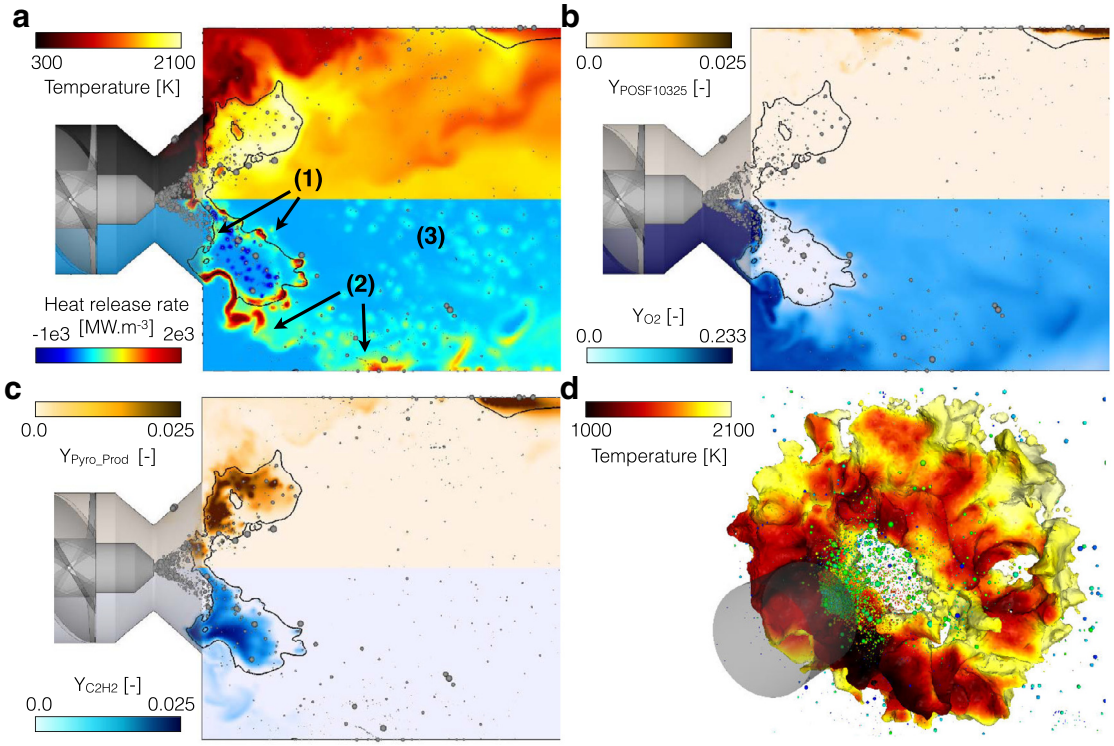

Fig. 11. Instantaneous fields in a central z-normal cut plane in reacting conditions. (a) Temperature (top) and heat release rate (bottom), (b) fuel mass fraction (top) and O_2 mass fraction (bottom), (c) pyrolysis products mass fraction (top) and C_2H_2 mass fractions (bottom) and (d) 3D-view of the rich torus using a $Y_z = 0.8$ iso-surface. The black iso-line indicates stoichiometry

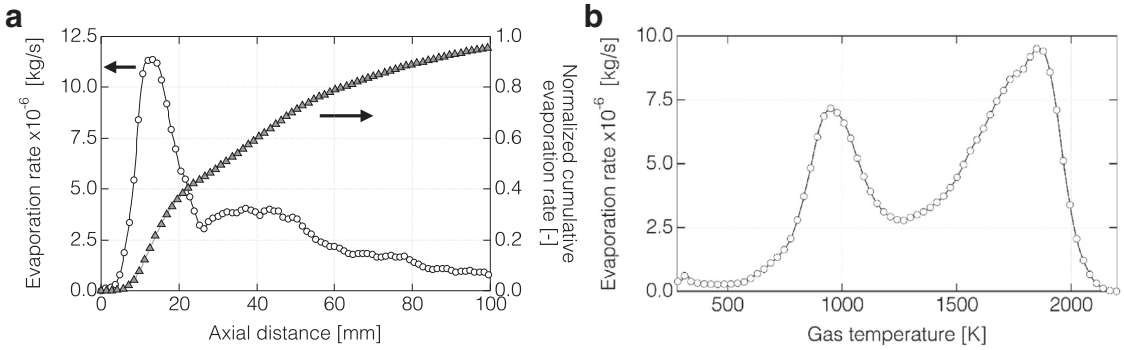

Fig. 12. (a)Time-averaged spatial evolution of evaporation rate in the axial direction, integrated in x-normal planes. (b) Time-averaged total evaporation rate versus gaseous temperature, in the first half of the combustion chamber.

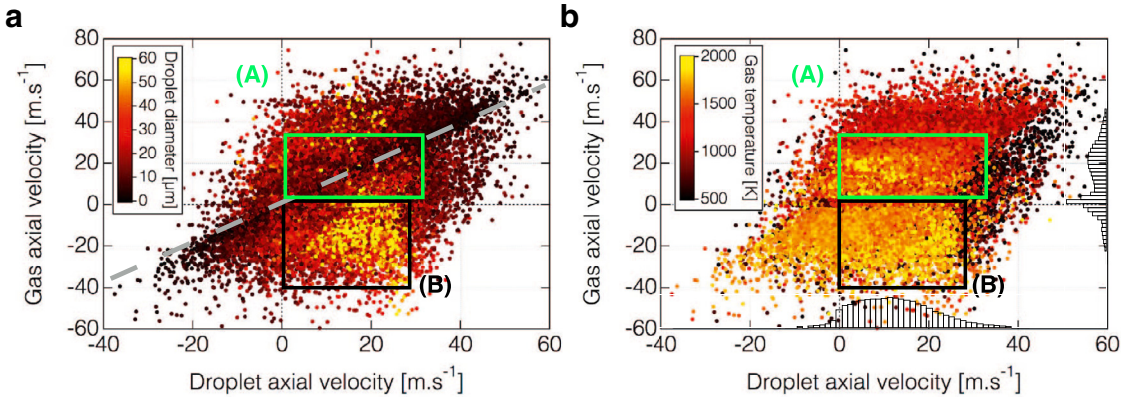

Fig. 13. Instantaneous scatterplots of gas axial velocity versus droplets axial velocity; colored by (a) droplets diameter and (b) gas temperature. All gas quantities are interpolated at the droplets position. Droplets are chosen such that they are located in zones were $T_{gas} > 400$ K. PDFs of gas axial velocity and droplets axial velocity are overlaid on (b). See text for details about the lines and frames. (For interpretation of the references to color in this figure legend, the reader is referred to the web version of this article.)

larger droplets is situated in regions with very high temperature levels (around 2000 K), only observed in the downstream part of the burned gas torus (see Fig. 11(a)). These droplets maintain a ballistic-like trajectory throughout the reaction zone (1) and burn as isolated droplets in the IRZ (reaction zone (3)). They are in part responsible for the plateau of evaporation rate seen in Fig. 12(a). Finally, the trace of droplets flowing in the ORZ with fresh gases is also identified in Fig. 13(b): such droplets exhibit a high positive axial velocity and are located in regions where the gaseous temperature is about 900 K corresponding to the flow conditions just upstream of flame fronts (2).

6.1.2. Flame structure analysis

In order to identify the combustion regimes of each reacting region, a Takeno index [82] is employed. The lack of unburnt gaseous fuel requires to adapt the definition of the Takeno index initially developed for a single-step global reaction. The spatial distribution of hydrocarbon species, shown in Fig. 11(c), indicates that intermediate species produced by the pyrolysis of Jet-A, as well as acetylene, are well suited to evaluate the combustion regimes. Thus, a lumped species, referred to as CS (Carbonated Species), is introduced. It is comprised of the fuel, pyrolysis products and acetylene:

$$Y_{CS} = Y_{POSF10325} + \sum_{pyro.prod.} Y_{pyro.prod.} + Y_{C_2H_2} \tag{17}$$

The Takeno index $\mathcal{I}_k$ is then defined by:

$$\mathcal{I}_k = \frac{\nabla Y_{CS} \cdot \nabla Y_{O_2}}{|\nabla Y_{CS}|.|\nabla Y_{O_2}|} \tag{18}$$

and displayed in the top part of Fig. 14(a). Negative values indicate a diffusion flame front, while positive values reveal a premixed flame front. The analysis of $\mathcal{I}_k$ distribution in the three aforementioned reaction zones, coupled with the species fields displayed in Fig. 11, enable to shed some light on the flame structures.

The flame front (1), located around the pocket of rich burnt gases, is in a diffusion regime. This flame can be further divided into a front diffusion flame ($D1_{front}$) and a back diffusion flame ($D1_{back}$), depending upon the oxidizer characteristics, as seen in Fig. 11(a) and (b): while the front flame oxidizer is fresh air, the back flame burns with recirculated lean mixtures at moderate temperature (around 1600 K).

The flame front (2) is mainly of a premixed nature. It consumes a mixture composed of fresh air diluted with burnt gases, vaporized fuel and pyrolysis products in small quantities; up to an equivalence ratio of 0.3. The latter is below the flammability limit of the Jet-A/air mixture at the combustor inlet conditions but the dilution with hot burnt gases allows to sustain a premixed flame. The local temperature upstream the flame front is of about 900 K. Low temperature intermediate species such as HO_2 or H_2O_2 are also observed, in the corners of the combustion chamber, indicating that low temperature chemistry could occur upstream of the premixed front. It is believed that the complex mixture feeding the premixed flames (2) forms in the vicinity of the diffusion flame (1), where local intermittent quenching allows gases from the hot torus to leak into the fresh air stream. Note that the complexity of such premixed flames would not be accurately captured with a global chemical mechanism, due to a lack of intermediate species, nor with a tabulated chemistry, since the local equivalence ratio is

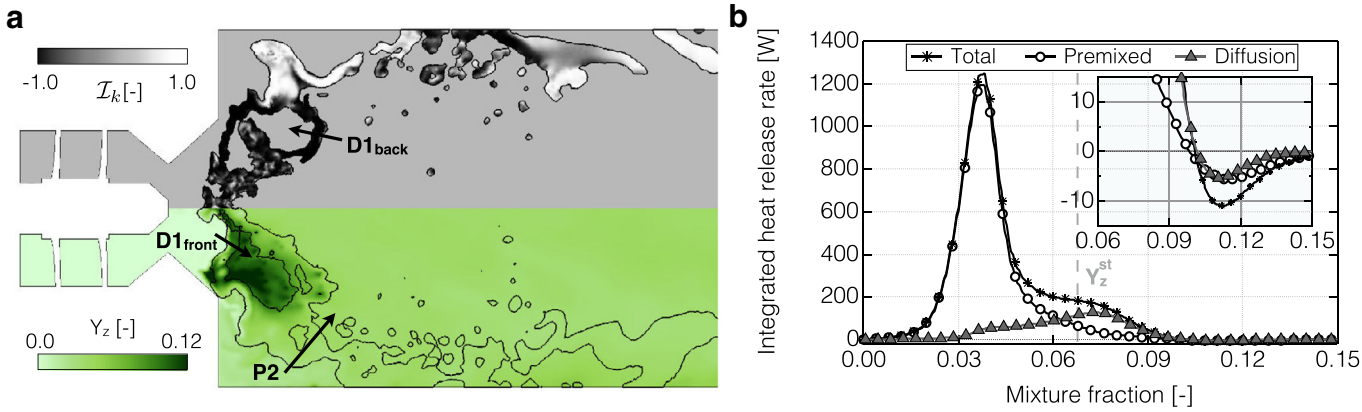

Fig. 14. (a) Instantaneous $\mathcal{I}_k$ field (top) and mixture fraction Y_z (bottom) in a central z-normal cut plane with overlaid iso-contours of heat release rate ($\dot{\omega}_T = 10^8$ W/m^3). Arrows indicate the position of the $z - T$ profiles, see Fig. 15. (b) Integrated heat release rate conditioned on mixture fraction $< \int_V \dot{\omega}_T \, dV | Y_z >$, with a close-up in the region $0.06 < Y_z < 0.15$.

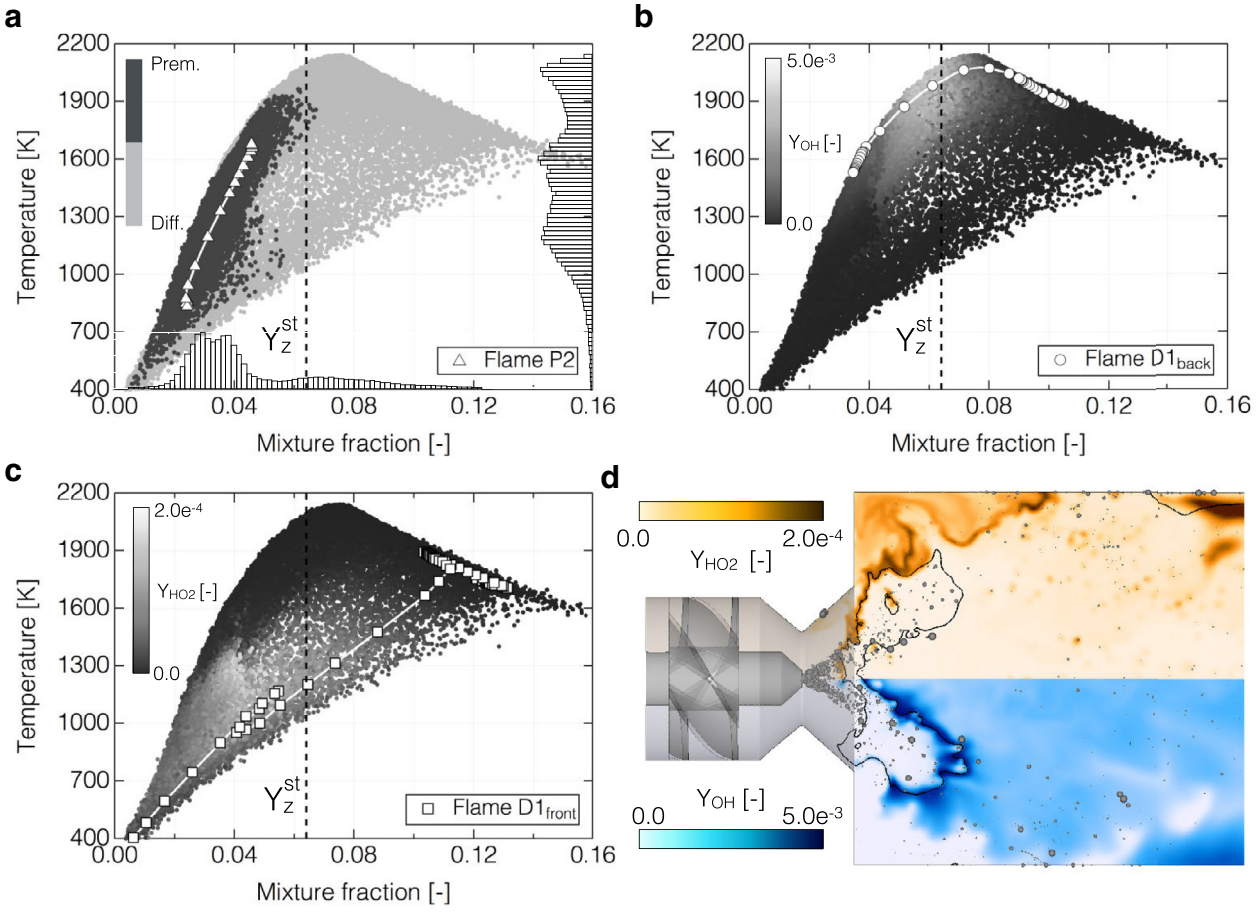

Fig. 15. Instantaneous scatterplots of gaseous temperature versus mixture fraction colored by $\mathcal{I}_k$ (a), OH species (b), and HO_2 species (c). Points are chosen close to the injector. Superimposed are trajectories across premixed (P2) and diffusion ($D1_{back}$, $D1_{front}$) flame fronts identified on Fig. 14(a). PDFs of mixture fraction and temperature are overlaid on (a). Instantaneous fields of OH and HO_2 mass fraction in a central z-normal cut plane (d).

below the flammability limit of the POSF10325 at the combustor inlet.

Finally, the individual droplets are found to burn in a complex regime (3) that will be discussed in Section 6.1.3.

To analyze the contributions of the premixed and diffusion flame fronts to the overall heat release rate, a volumetric integration is performed, conditioned on Y_z and differentiated with $\mathcal{I}_k$. Results are displayed in Fig. 14(b). The heat release rate is spread over a wide range of mixture fraction, characteristic of partially-premixed combustion. Most of the heat release occurs on the lean side, with a peak at an equivalence ratio of 0.6 ($Y_z = 0.037$), lower than the global equivalence ratio of 0.75. The contribution from premixed flame fronts is found to be largely dominant. This finding is consistent with previous DNS studies of similar flames [6]. In the present study, it is attributed to the large observed intermittency of the diffusion fronts. The peak of integrated heat re-

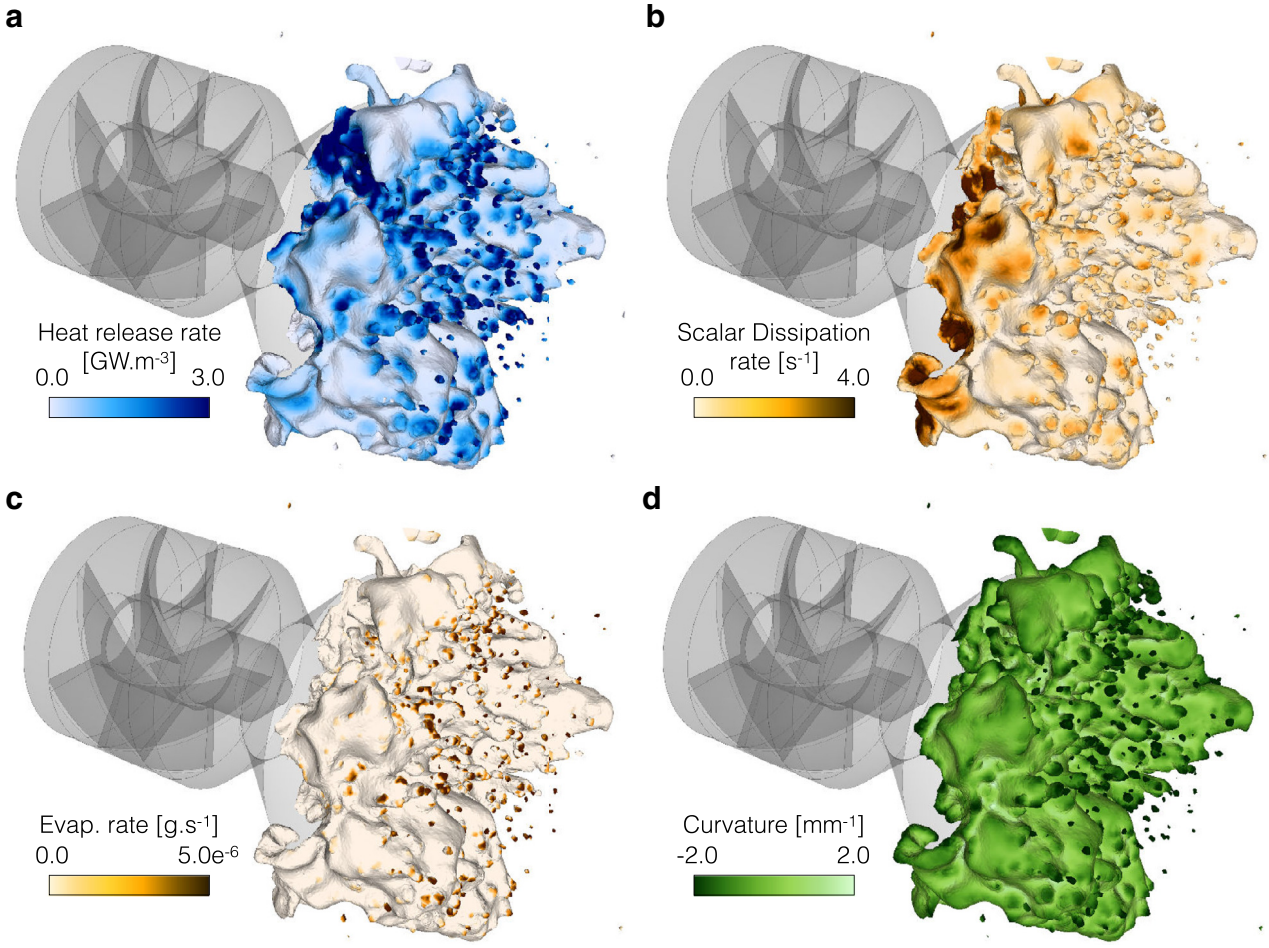

Fig. 16. Iso-surface of stoichiometric mixture fraction, colored by (a) heat release rate, (b) χ, (c) evaporation rate and (d) curvature.

lease associated with diffusion flames is slightly skewed towards rich mixtures and spreads over a wider range of mixture fractions compared to purely gaseous diffusion flames. This is the consequence from the interaction between the spray and the reaction zone (1), as will be further discussed in Section 6.1.3. Finally, note that negative integrated heat release is observed for rich mixtures, which is the signature of endothermic reactions associated with the rapid pyrolysis of the fuel (also visible in Fig. 11(a)). This has already been observed in DNS of spark ignition in droplet clouds [83].

Scatterplots of gaseous temperature versus mixture fraction are shown in Fig. 15(a)–(c). Practically all premixed flame structures, identified with dark symbols in Fig. 15(a), are found to locate on the lean side. Additionally, a high degree of mixture stratification is observed, as illustrated by the trajectory of the premixed flame P2 identified in the bottom part of Fig. 14(a), and as triangles in Fig. 15(a). The diffusion structures, identified with light gray symbols, are found to cover a larger portion of the mixture fraction space. However, the probability density function (PDF) of Y_z overlaid in Fig. 15(a) indicates that they are less frequent than premixed structures.

In order to identify the traces of both the front and back diffusion flames discussed earlier, two trajectories are considered, as depicted in Fig. 14(a). The trajectory of $D1_{back}$ is reported with circles in Fig. 15(b), where it is seen to cross a region of relatively high concentration of OH species around stoichiometry. The trajectory of $D1_{front}$, reported with squares in Fig. 15(c), is seen to cross a region of relatively high concentration of HO_2 species on the lean side, and to lie very far from equilibrium. Both trajectories are representative of the entire front and back diffusion flame (1), as can be seen in Fig. 15(d). The presence of HO_2 is usually associated with low temperature chemistry and extinction event, revealing that the front diffusion flame is highly strained: compared to the back diffusion flame, the front flame is subjected to higher turbulence (see Fig. 7(b)) as well as to a higher Y_z gap in-between the oxidizer and fuel sides.

The three trajectories P2, $D1_{back}$ and $D1_{front}$ are seen to encompass the bulk of the data, as they are "limiting case" examples. In particular, the front and back diffusion flame (1) trajectories are seen to merge on the rich mixing line in Fig. 15(b) and (c), representative of the activity inside the rich, hot torus.

6.1.3. Spray-flame interactions

The primary effect of evaporation on the Y_z field is the increased heterogeneity, leading to flame wrinkling induced by the crossing of large droplets, mainly seen on $D1_{back}$, as reported in Fig. 16. This is consistent with experimental observations by Mercier et al. [84]. As a result, the stoichiometric iso-surface exhibits small hills of very high negative curvature (Fig. 16(d)). Isolated spheric structures are also clearly visible. The curvature is here defined as $\nabla \cdot \boldsymbol{n}_z$, where $\boldsymbol{n}_z = \nabla Y_z / |\nabla Y_z|$ is pointing towards rich regions. Figure 16(b) displays the resolved scalar dissipation rate on the stoichiometric iso-surface, defined as:

$$\chi_{st} = 2D|\nabla Y_z^{st}|^2 \tag{19}$$

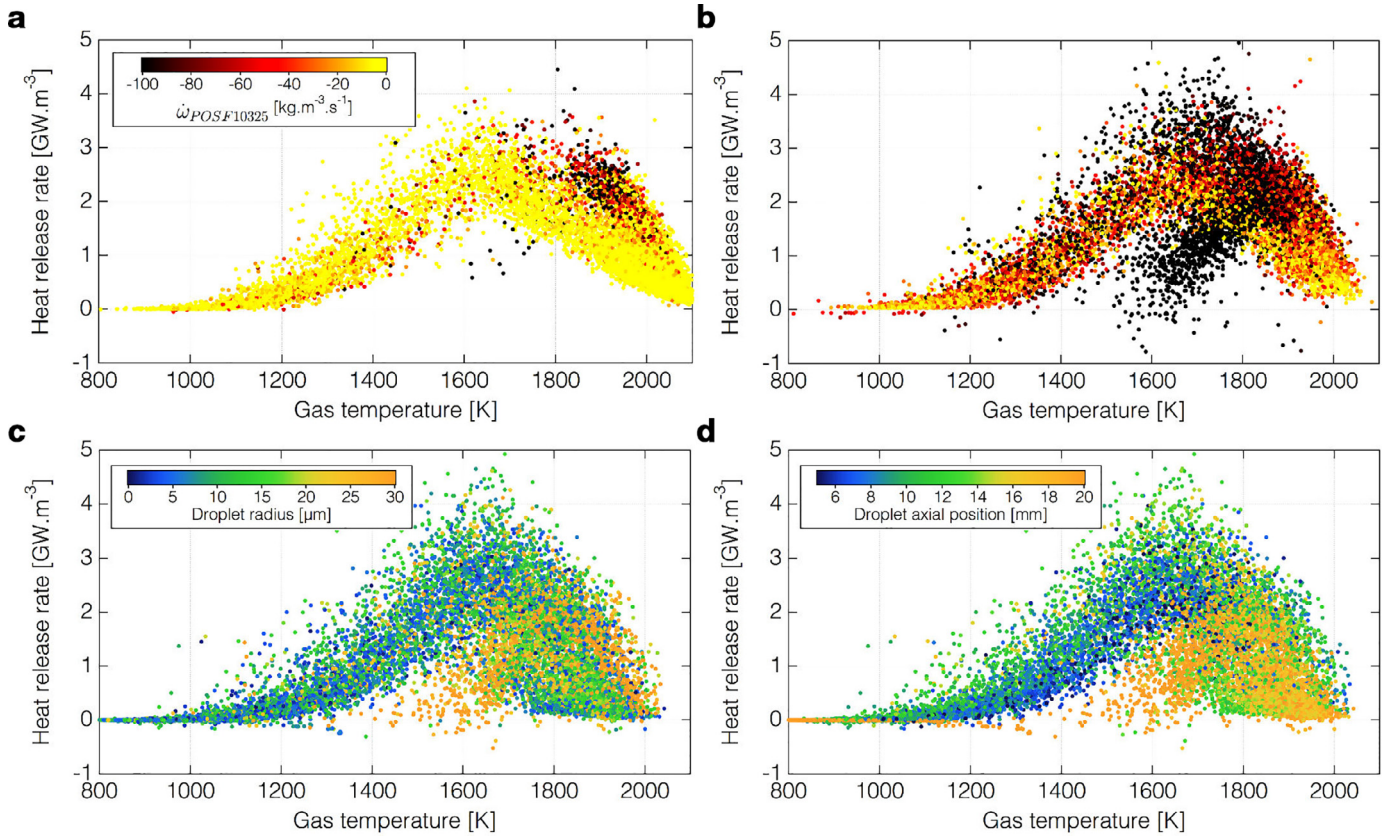

Fig. 17. (a) and (b): instantaneous scatterplots of heat release rate versus temperature; colored by the source term of fuel. Points are chosen at stoichiometry, and such that the evaporation term source is (a) $< 10^{-10}$ kg.s^{-1} or (b) $> 10^{-10}$ kg.s^{-1}. (c) and (d): instantaneous scatterplots of gas heat release rate versus gas temperature interpolated at droplets position; colored by (c) the droplet radius, (d) the droplet axial position. Points are chosen at stoichiometry, and such that the evaporation term source is $> 10^{-10}$ kg.s^{-1}.

As expected, high χ_{st} values above 4 s^{-1} and close to the extinction value of 10.5 s^{-1} (Fig. 3 (f)) are observed on D1$_{front}$. The highly curved regions on D1$_{back}$, however, appear to have a limited correlation with χ_{st}. Since the correlation between the heat release rate and curvature is apparent (Fig. 16(a)), it is concluded that, as opposed to what is expected from gaseous flame theory, the local flame intensity D1$_{back}$ is not primarily controlled by the scalar dissipation rate. In fact, the contribution from evaporation to the total fuel flux at stoichiometry can supersede that of the diffusion flux (evaluated by the level of χ_{st}), especially in low scalar dissipation rate zones. To confirm this analysis, Fig. 16(c) shows that the evaporation rate is locally strong around droplets and is well correlated with the heat release rate.

Figure 17 reports scatterplots of heat release rate versus gaseous temperature, for points located on the iso-surfaces depicted in Fig. 16. Four graphs are displayed: Fig. 17(a) and (b) are composed of points at the grid nodes where the evaporation source term is either negligible (a) or relatively important (b); Fig. 17(c) and (d) are constructed from interpolation of the gaseous variables at the droplets position and limited to locations where the evaporation source term is relatively important. Figure 17(a) and (b) are colored by the source term of fuel, Fig. 17(c) is colored by the droplets radius, and Fig. 17(d) is colored by the droplets axial position. The points distribution is similar in all graphs, except in the 1600–1800 K range where a tilted "V-like" structure of points characterized by high fuel consumption rate appears in the plots associated to strong evaporation (Fig. 17(b)–(d)): this corresponds to fuel pyrolysis, which occurs very quickly after evaporation.

The lower branch of the tilted V-structure is composed of points surrounding large evaporating isolated droplets (Fig. 17(c) and (d)), located right behind flame (1) (entering reaction zone (3)). The low heat release rate indicates that the fast pyrolysis of large quantities of fuel is not balanced by the slower oxidation of the pyrolysis products. At the same time, the temperature is reduced due to the strong evaporation. The frequent occurrence of such isolated droplet combustion calls for specific models, as proposed, e.g. in [73], which were not considered in this work. As a consequence, although the occurrence of such burning regime is well captured, the exact associated flame structures are not necessarily properly described.

The top branch is composed of points with high heat release rate. The associated droplets radius and axial position allows to identify these points as part of the wrinkled structures seen on the back diffusion flame front (1), displayed in Fig. 16. In this case, even if evaporation has a tendency to draw energy from the gaseous phase, the addition of fuel to the already burning flame front is enough to compensate for the loss, and even to locally enhance the heat release rate.

6.2. Pollutant formation

6.2.1. CO species

The CO source term $\dot{\omega}_{CO}$ and CO mass fraction fields are displayed in Fig. 18(a) and (b), respectively. As expected from the locally rich conditions, CO is largely produced in the diffusion fronts (1), particularly in the back diffusion front exhibiting the highest temperature levels. Locally, CO production is also boosted by the evaporation of fuel, as revealed by the clouds of CO production

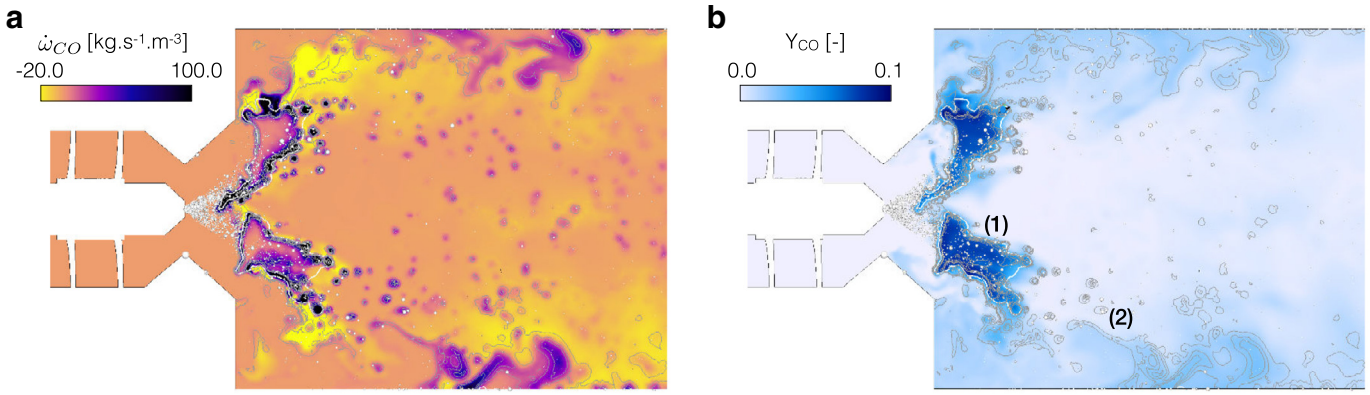

Fig. 18. Instantaneous fields of (a) CO source term and (b) CO mass fraction in a central z-normal cut place with overlaid droplets and iso-contours of heat release rate (grey) and stoichiometry (white).

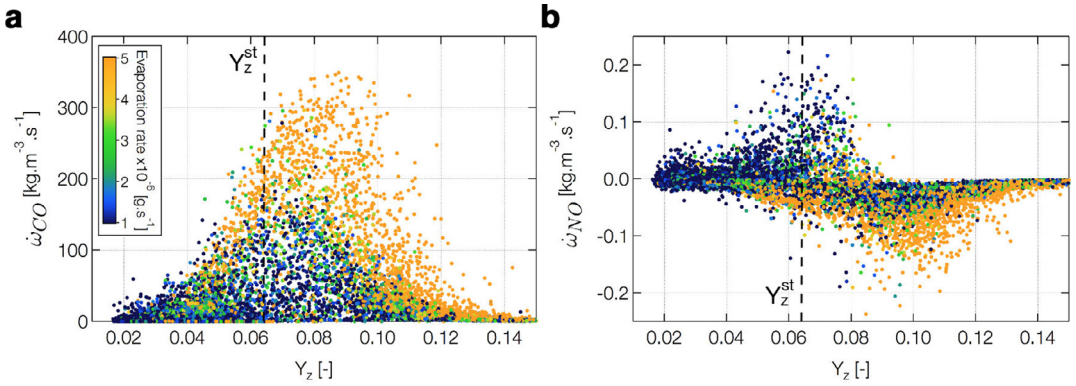

Fig. 19. Scatterplots of (a) CO source term and (b) NO source term versus mixture fraction, colored by the evaporation rate. Points are restricted to the diffusion front (1) with $T > 800$ K.

following evaporating isolated droplets. This is especially true for droplets located right behind the stoichiometric iso-contours. This is best put forward in Fig. 19(a) showing a scatterplot of CO production versus mixture fraction, colored by the evaporation source term.

The CO produced in the diffusion front (1) is stored in the burnt gas torus, where intermittent extinctions allow pockets of rich burnt gases to leak into the cold air stream (see the combustion chamber corners in Fig. 18(b)). CO mass fraction close to 0.03 can then be observed on the fresh side of the premixed flame fronts (2), explaining the relatively high CO consumption observed before $x = 50$ mm. Finally, a non-negligible amount of CO production occurs also in premixed fronts located further downstream in the combustion chamber, near the walls. Indeed, impacting evaporating droplets around $x = 50$ mm allow a sufficient increase of the local equivalence ratio and feed additional pyrolysis products to the lean premixed flame fronts; locally modifying the premixed structure from CO consuming to CO producing. This is consistent with the high CO mass fraction observed close to the walls on the time-averaged profiles in both LES and experiment (see Fig. 9).

6.2.2. NO species

It is interesting to differentiate and quantify the NO production related to fast flame processes, which are strongly dependent upon the local conditions, from that occurring in post-flame regions, associated with slower timescales and bearing a more universal nature. This is usually done by investigating the reaction pathways involving the NO species, namely the Zeldovich (thermal), the Prompt and the N_2O routes [85,86]. The NNH route can also become quite important in the burnt gases under relatively low temperatures [87]. Note that in the ARC_29_JetANOx mechanism employed in this work, the N_2O route is not included. Indeed, it is usually argued that this route is important only under fuel lean/high pressure conditions. The configuration under investigation here operating at atmospheric pressure, the chemistry reduction identified it as being insignificant. The NNH route, on the contrary, is conserved.

Figure 20 presents the NO source term as well as the contribution from the Zeldovich, Prompt and NNH routes, in a z-normal central cut plane. These routes are identified based on specific reactions and associated pathways, as prescribed on the aforementionned publications (the reactions employed in each route are listed in Appendix C). Like CO, NO is seen to be mainly produced in the back diffusion flame front (1). The main contribution to the net production in this high temperature region is from the Zeldovich mechanism (Fig. 20(b)). The contribution from the NNH pathway is exclusively positive (no consumption), and is also not negligible (Fig. 20(d)). Interestingly, NO is largely reburnt inside the rich torus, and the pathway analysis reveals that this is primarily due to the consumption pathways included in the Prompt mechanism. In particular, some NO is also consumed by the Prompt mechanism in the front diffusion flame (1); however no NO is produced in this flame front where the relatively high NO levels are due to diffusion. As suggested by the very negative NO consumption rate surrounding isolated droplets seen in Fig. 20(c), evaporation increases the NO reburn under rich conditions. This is evidenced in Fig. 19(b), showing a scatterplot of NO production versus mixture fraction, colored by the evaporation source term.

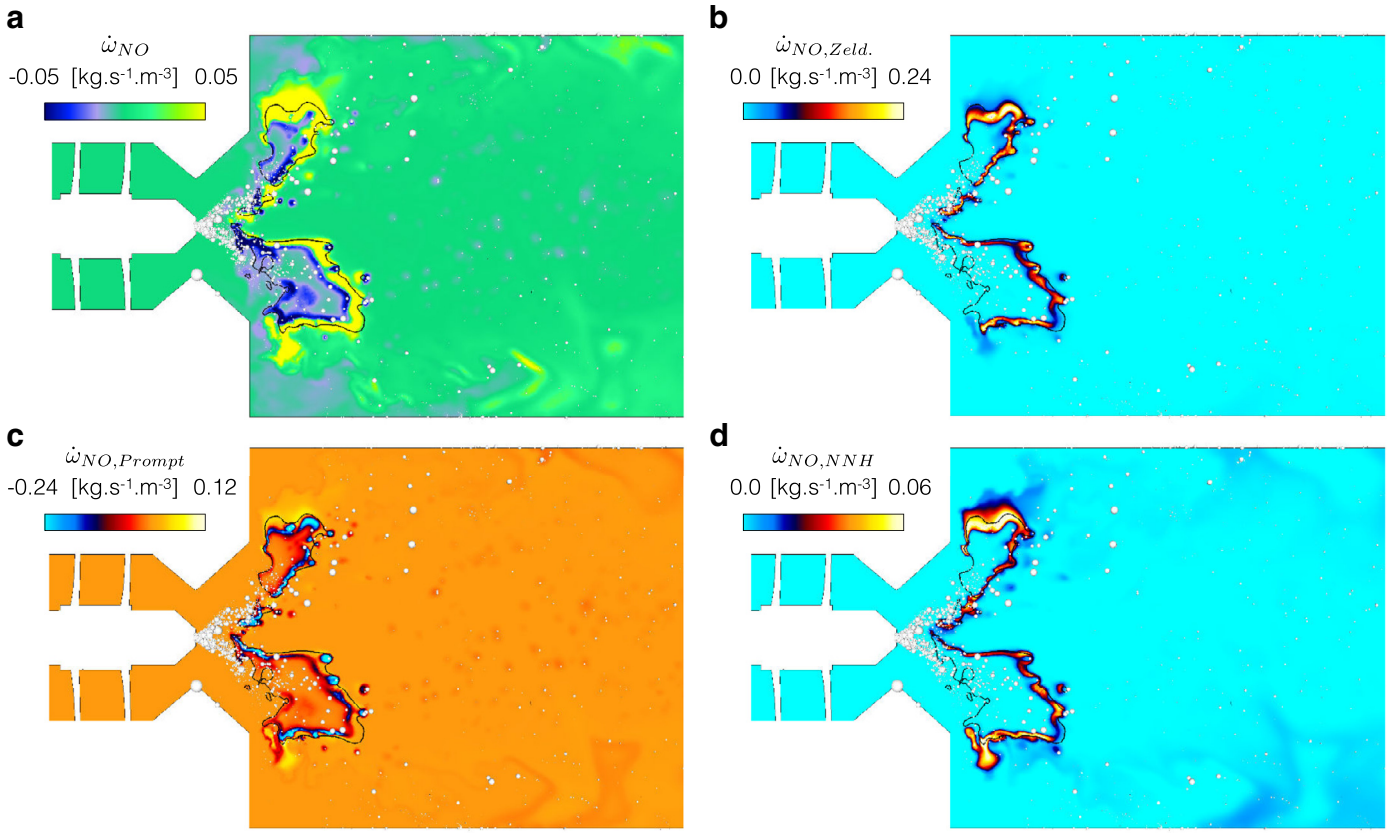

Fig. 20. Instantaneous fields of (a) source term of NO with decomposition into (b) Zeldovich (thermal) pathway, (b) Prompt pathway and (c) NNH pathway.

Note that some NO formation is seen to occur in the lean premixed flame fronts (2) in Fig. 20(a). If part of this formation is imputable to the NNH pathway, there are obviously non-negligible contributions from additional pathways which are not considered in any of the aforementioned three routes. Likewise, none of the route considered is able to explain the NO reburn seen on the corner of the combustion chambers in Fig. 20(a). Hence, a complete description of the NO formation, including secondary pathways, is necessary to predict NO concentrations under certain circumstances. As demonstrated here, ARCs provide a very efficient framework in such a case.

7. Conclusion

In this paper, LES of a two-phase flow lean direct-injection system operated with real aeronautical fuel is performed. The main intent is to evaluate the feasibility of a new methodology to accommodate such fuels in LES, in order to improve predictive capabilities in terms of flame structure and pollutant formation. The approach combines the direct integration of a real Jet-A fuel description, relying on the recently proposed hybrid chemistry (HyChem) model. Direct integration of the chemistry in the LES is accomplished through an LES-compliant Analytically Reduced Chemistry (ARC) comprised of 29 transported species, within a thickened flame chemistry-interaction framework (DTFLES). A Lagrangian spray description is employed. The ARC mechanism is first validated in canonical archetypes representative of the flame configuration under consideration, before being implemented in the LES solver AVBP. With this approach, no additional modeling assumptions about the flow or flame structure are required.

A good agreement is observed between the LES results and the experimental data in terms of velocity fields and spray characteristics. Comparisons with temperature and species data further validate the methodology. In particular, results demonstrate the improved predictive capabilities, when compared to previous LES studies of the same configuration, employing either tabulation [23] or an empirically fitted global scheme [12]. The level of description allows a detailed analysis of the spray flame structure: on top of the complex spatial arrangement of premixed and diffusion fronts already observed in DNS [6], transport and differential diffusion of intermediate species comprised in the ARC result in a variety of mixture compositions. For example, it was observed that the main diffusion flame is principally fueled by pyrolysis products such as C_2H_2, and that the composition of the weak premixed flame fronts alongside the walls are mainly fueled by the CO resulting from the mixing of fresh air with the rich burnt products of the main diffusion flame. Additionally, it was shown that the direct interactions of the spray with the diffusion flame fronts strongly affect the flame structure, locally increasing the production of CO and causing NO reburning.

The results confirm that the ARC-DTFLES methodology is well suited for HyChem models, thus opening new perspectives for LES of industrial kerosene fueled configurations. Further work will concentrate on assessing the capabilities of the method to capture fuel effects (other petroleum based fuels or biofuels) on the flame structure and pollutant emissions. The flame structure observed in such direct injection systems also reveals individual droplet burning for which specific LES models need to be included. Finally, note that the use of HyChem within the ARC framework is not restricted to the DTFLES model, and other combustion models directly including chemical kinetics could benefit from this approach.

Acknowledgments

The authors would like to thank P. Pepiot from Cornell for fruitful collaboration. This work was performed using HPC resources

from GENCI-CCRT (Grant no. 2016-2b7525). The authors would like to acknowledge the support of the Center for Turbulence Research (Stanford University - NASA Ames Research Center) as this work has been initiated during the 2016 Summer Program of this institute. The research at Stanford was funded by the Air Force Office of Scientific Research under Grant nos. FA9550-14-1-0235 and FA9550-16-1-0195 and by the National Aeronautics and Space Administration (NASA) under agreement numbers NNX15AV05A.

Appendix A. Specification transported species Schmidt number

See Table A1

Table A1
Species contained in the ARC_29_JetA2NOx scheme.

Species	N_2	H	H_2	HO_2	H_2O	H_2O_2	O	O_2
Sc_k	0.69	0.12	0.20	0.74	0.54	0.74	0.48	0.73
Species	OH	CO	CO_2	CH_3	CH_4	CH_2O	CH_2CO	
Sc_k	0.48	0.74	0.94	0.67	0.67	0.85	1.00	
Species	C_2H_2	C_2H_4	C_2H_6	C_3H_6	I-C_4H_8	C_5H_6	$C_6H_4O_2$	
Sc_k	0.87	0.88	0.97	1.24	1.40	1.44	1.67	
Species	C_6H_5O	C_6H_6	$C_6H_5CH_3$	POSF10325	NO	HCN	NO_2	
Sc_k	1.58	1.55	1.73	2.40	0.75	0.85	0.84	

Appendix B. List of pyrolysis reactions for the Jet-A POSF10325

Following the HyChem methodology, the fuel breakdown is described by several lumped reactions. For the Jet-A (POSF10325) fuel (Version I), 6 reactions are considered. They are:

$$(1) - POSF10325 \rightarrow 2.95\ C_2H_4 + 0.39\ C_3H_6 + 0.195\ \text{i-}C_4H_8 + 0.1833\ C_6H_6 + 0.15\ C_6H_5CH_3 + H + CH_3$$

$$(2) - POSF10325 + H \rightarrow H_2 + 0.05\ CH_4 + 2.83083\ C_2H_4 + 0.48616\ C_3H_6 + 0.243083\ \text{i-}C_4H_8 + 0.1925\ C_6H_6 + 0.1575\ C_6H_5CH_3 + 0.4\ H + 0.6\ CH_3$$

$$(3) - POSF10325 + CH_3 \rightarrow 1.05\ CH_4 + 2.83083\ C_2H_4 + 0.48616\ C_3H_6 + 0.243083\ \text{i-}C_4H_8 + 0.1925\ C_6H_6 + 0.1575\ C_6H_5CH_3 + 0.4\ H + 0.6\ CH_3$$

$$(4) - POSF10325 + OH \rightarrow H_2O + 0.05\ CH_4 + 2.83083\ C_2H_4 + 0.48616\ C_3H_6 + 0.243083\ \text{i-}C_4H_8 + 0.1925\ C_6H_6 + 0.1575\ C_6H_5CH_3 + 0.4\ H + 0.6\ CH_3$$

$$(5) - POSF10325 + O_2 \rightarrow HO_2 + 0.05\ CH_4 + 2.83083\ C_2H_4 + 0.48616\ C_3H_6 + 0.243083\ \text{i-}C_4H_8 + 0.1925\ C_6H_6 + 0.1575\ C_6H_5CH_3 + 0.4\ H + 0.6\ CH_3$$

$$(6) - POSF10325 + HO_2 \rightarrow H_2O_2 + 0.05\ CH_4 + 2.83083\ C_2H_4 + 0.48616\ C_3H_6 + 0.243083\ \text{i-}C_4H_8 + 0.1925\ C_6H_6 + 0.1575\ C_6H_5CH_3 + 0.4\ H + 0.6\ CH_3$$

Their associated reaction rates are provided in Table B1.

Since the current work started, a newer version of the HyChem model for the Jet-A fuel has been made available. Details of the model is described in refs. [46,47]. The two versions of the Jet-A model give similar predictions for global combustion properties, including ignition delay, laminar flame speeds, and non-premixed flame extinction strain rate.

Table B1
Reaction rate parameters associated to the Jet-A (POSF10325) fuel (Version I).

Reac. nb.	Pre-exponential factor	Temperature exponent	Activation energy
	[$cm^a.mol^b.s^c$]	[-]	[$cal.mol^{-1}$]
(1)	5.86×10^{25}	−2.66	88207.0
(2)	1.53×10^{-1}	4.76	1294.9
(3)	9.52×10^{-7}	5.95	4748.4
(4)	3.55×10^{10}	1.02	213.2
(5)	2.55×10^{14}	0.06	47532.6
(6)	2.33×10^{4}	2.94	14810.0

Appendix C. List of reactions considered in the NOx pathway analysis

See Tables C1–C3

Table C1
Reactions considered in the Zeldovich route.

$N + OH \rightleftarrows NO + H$
$N_2 + O \rightleftarrows N + NO$
$N + O_2 \rightleftarrows NO + O$

Table C2
Reactions considered in the Prompt route.

$HCN + H2O \rightleftarrows CH_3 + NO$
$HCN + O \rightleftarrows CH + NO$
$HCN + HCO \rightleftarrows C_2H_2 + NO$
$NCO + O \rightleftarrows NO + CO$
$NCO + OH \rightleftarrows NO + HCO$
$NCO + O_2 \rightleftarrows NO + CO_2$
$NO_2 + CH \rightarrow HCO + NO$
$NO_2 + CO \rightarrow CO + 2.0\ NO$
$HCCO + NO \rightarrow HCN + CO_2$
$CH2^* + NO \rightarrow HCN + OH$
$CH2 + NO \rightarrow HCN + OH$

Table C3
Reactions considered in the NNH route.

$NH + O \rightleftarrows NO + H$
$NH + O_2 \rightleftarrows NO + OH$

References

[1] L.Y.M. Gicquel, G. Staffelbach, T.J. Poinsot, Large eddy simualtions of gaseous flames in gas turbine combustion chambers, Prog. Energy Combust. Sci. 38 (6) (2012) 782–817.
[2] T. Lu, C.K. Law, Toward accommodating realistic fuel chemistry in large-scale computations, Prog. Energy Combust. Sci. 35 (2) (2009) 192–215.
[3] B. Fiorina, D. Veynante, S. Candel, Modeling combustion chemistry in large eddy simulation of turbulent flames, Flow, Turbul. Combust. 94 (2015) 3–42.
[4] A.L. Sánchez, J. Urzay, A. Liñán, The role of separation of scales in the description of spray combustion, Proc. Combust. Inst. 35 (2) (2015) 1549–1577.
[5] J. Reveillon, L. Vervisch, Analysis of weakly turbulent dilute-spray flames and spray combustion regimes, J. Fluid Mech. 537 (2005) 317–347.
[6] K. Luo, H. Pitsch, M.G. Pai, O. Desjardins, Direct numerical simulations and analysis of three-dimensional n-heptane spray flames in a model swirl combustor, Proc. Combust. Inst. 33 (2) (2011) 2143–2152.
[7] C.K. Westbrook, F.L. Dryer, Simplified reaction mechanisms for the oxidation of hydrocarbon fuels in flames, Combust. Sci. Technol. 27 (1981) 31–43.
[8] W.P. Jones, R.P. Lindstedt, Global reaction schemes for hydrocarbon combustion, Combust. Flame 73 (3) (1988) 233–249.

[9] W.P. Jones, A. Tyliszczack, Large eddy simulation of spark ignition in a gas turbine combustor, Flow Turbul. Combust. 85 (3-4) (2010) 711–734.
[10] C. Fureby, A comparative study of flamelet and finite rate chemistry LES for a swirl stabilized flame, J. Eng. Gas Turb. Power 134 (4) (2012) 041503.
[11] M. Philip, M. Boileau, R. Vicquelin, E. Riber, T. Schmitt, B. Cuenot, D. Durox, S. Candel, Large eddy simulations of the ignition sequence of an annular multiple-injector combustor, Proc. Combust. Inst. 35 (3) (2015) 3159–3166.
[12] N. Patel, S. Menon, Simulation of spray–turbulence–flame interactions in a lean direct injection combustor, Combust. Flame 153 (1) (2008) 228–257.
[13] G. Hannebique, P. Sierra, E. Riber, B. Cuenot, Large eddy simulation of reactive two-phase flow in an aeronautical multipoint burner, Flow, Turbul. Combust. 90 (2) (2013) 449–469.
[14] M. Bauerheim, T. Jaravel, L. Esclapez, E. Riber, L.Y.M. Gicquel, B. Cuenot, M. Cazalens, S. Bourgois, M. Rullaud, Multiphase flow large-eddy simulation study of the fuel split effects on combustion instabilities in an ultra-low-nox annular combustor, J. Eng. Gas Turb. Power 138 (6) (2016) 061503.
[15] B. Franzelli, E. Riber, M. Sanjose, T. Poinsot, A two-step chemical scheme for kerosene–air premixed flames, Combust. Flame 157 (7) (2010) 1364–1373.
[16] N. Peters, Laminar diffusion flamelet models in non-premixed turbulent combustion, Prog. Energy Combust. Sci. 10 (3) (1984) 319–339.
[17] J.A.V. Oijen, F.A. Lammers, L.P.H.D. Goey, Modeling of complex premixed burner systems by using flamelet-generated manifolds, Combust. Flame 127 (3) (2001) 2124–2134.
[18] O. Gicquel, N. Darabiha, D. Thévenin, Laminar premixed hydrogen/air counterflow flame simulations using flame prolongation of ILDM with differential diffusion, Proc. Combust. Inst. 28 (2) (2000) 1901–1908.
[19] C.D. Pierce, P. Moin, Progress-variable approach for large-eddy simulation of non-premixed turbulent combustion, J. Fluid Mech. 504 (2004) 73–97.
[20] Y.C. See, M. Ihme, Large eddy simulation of a partially-premixed gas turbine model combustor, Proc. Combust. Inst. 35 (2) (2015) 1225–1234.
[21] B. Franzelli, A. Vié, M. Ihme, On the generalisation of the mixture fraction to a monotonic mixing-describing variable for the flamelet formulation of spray flames, Combust. Theory Model. 19 (6) (2015) 773–806.
[22] L. Esclapez, P.C. Ma, E. Mayhew, R. Xui, S. Stouffer, T. Lee, H. Wang, M. Ihme, Fuel effects on lean blow-out in a realistic gas turbine combustor, Combust. Flame 181 (2017) 82–99.
[23] E. Knudsen, H. Pitsch, Modeling partially premixed combustion behavior in multiphase LES, Combust. Flame 162 (1) (2015) 159–180.
[24] B. Franzelli, B. Fiorina, N. Darabiha, A tabulated chemistry method for spray combustion, Proc. Combust. Inst. 34 (1) (2013) 1659–1666.
[25] C. Hollmann, E. Gutheil, DifSr spray flame library, Combust. Sci. Technol. 135 (1–6) (1998) 175–192.
[26] H. Olguin, E. Gutheil, Influence of evaporation on spray flamelet structures, Combust. Flame 161 (4) (2014) 987–996.
[27] Y. Hu, H. Olguin, E. Gutheil, Transported joint PDF simulation of turbulent spray flames combined with a spray flamelet model using a transported scalar dissipation rate, Combust. Sci. Technol. 189 (2) (2016) 322–339.
[28] M. Ihme, H. Pitsch, Modeling of radiation and nitric oxide formation in turbulent nonpremixed flames using a flamelet/progress variable formulation, Phys. Fluids 20 (5) (2008) 055110.
[29] M.E. Mueller, H. Pitsch, LES model for sooting turbulent nonpremixed flames, Combust. Flame 159 (6) (2012) 2166–2180.
[30] D.A. Goussis, U. Maas, Model reduction for combustion chemistry, in: T. Echekki, E. Mastorakos (Eds.), Turbulent Combustion Modeling, Fluid Mechanics and Its Applications, 95 (2011), pp. 193–220.
[31] A. Triantafyllidis, E. Mastorakos, R. Eggels, Large eddy simulation of forced ignition of a non premixed bluff-body methane flame with conditional moment closure, Combust. Flame 156 (2009) 2328–2345.
[32] G. Bulat, W.P. Jones, A.J. Marquis, Large eddy simulation of an industrial gas–turbine combustion chamber using the sub-grid pdf method, Proc. Combust. Inst. 34 (2) (2013) 3155–3164.
[33] T. Jaravel, E. Riber, B. Cuenot, G. Bulat, Large eddy simulation of an industrial gas turbine combustor using reduced chemistry with accurate pollutant prediction, Proc. Combust. Inst. 36 (3) (2017) 3817–3825.
[34] B. Franzelli, A. Vié, M. Boileau, B. Fiorina, N. Darabiha, Large eddy simulation of swirled spray flame using detailed and tabulated chemical descriptions, Flow Turbul. Combust. 98 (2) (2017) 633–661.
[35] A. Giusti, E. Mastorakos, Detailed chemistry LES/CMC simulation of a swirling ethanol spray flame approaching blow-off, Proc. Combust. Inst. 36 (2) (2017) 2625–2632.
[36] T. Edwards, Kerosene fuels for aerospacepropulsion—composition and properties, AIAA Paper 3874(2002).
[37] T. Edwards, L.Q. Maurice, Surrogate mixtures to represent complex aviation and rocket fuels, J. Propuls. Power 17 (2) (2001) 461–466.
[38] C. Wood, V. McDonell, R. Smith, G. Samuelsen, Development and application of a surrogate distillate fuel, J. Propuls. Power 5 (4) (1989) 399–405.
[39] A. Violi, S. Yan, E.G. Eddings, A.F. Sarofim, S. Granata, T. Faravelli, E. Ranzi, Experimental formulation and kinetic model for jp-8 surrogate mixtures, Combust. Sci. Technol. 174 (11-12) (2002) 399–417.
[40] P. Dagaut, M. Cathonnet, The ignition, oxidation, and combustion of kerosene: a review of experimental and kinetic modeling, Prog. Energy Combust. Sci. 32 (1) (2006) 48–92.
[41] W.J. Pitz, C.J. Mueller, Recent progress in the development of diesel surrogate fuels, Prog. Energy Combust. Sci. 37 (3) (2011) 330–350.
[42] S. Dooley, S.H. Won, M. Chaos, J. Heyne, T.I. Farouk, Y. Ju, F.L. Dryer, K. Kumar, X. Hui, C.-J. Sung, H. Wang, et al., The experimental evaluation of a methodology for surrogate fuel formulation to emulate gas phase combustion kinetic phenomena, Combust. Flame 159 (4) (2012) 1444–1466.
[43] K. Narayanaswamy, H. Pitsch, P. Pepiot, A component library framework for deriving kinetic mechanisms for multi-component fuel surrogates: Application for jet fuel surrogates, Combust. Flame 165 (2016) 288–309.
[44] D. Kim, J. Martz, A. Violi, A surrogate for emulating the physical and chemical properties of conventional jet fuel, Combust. Flame 161 (6) (2014) 1489–1498.
[45] A. Ahmed, G. Goteng, V.S. Shankar, K. Al-Qurashi, W.L. Roberts, S.M. Sarathy, A computational methodology for formulating gasoline surrogate fuels with accurate physical and chemical kinetic properties, Fuel 143 (2015) 290–300.
[46] H. Wang, R. Xu, K. Wang, C. Bowman, D. Davidson, R. Hanson, F. Egolfopoulos, A physics-based approach to modeling real-fuel combustion chemistry - I. Evidence from experiments, and thermodynamic, chemical kinetic andstatistical considerations., Combust. Flame (2017). submitted
[47] R. Xu, H. Wang, R. Hanson, D. Davidson, C. Browman, F. Egolfopoulos, Evidence supporting a simplified approach to modeling high-temperature combustion chemistry, 10th US National Meeting on Combustion, College Park, MD, 2017. submitted
[48] O. Colin, F. Ducros, D. Veynante, T. Poinsot, A thickened flame model for large eddy simulations of turbulent premixed combustion, Phys. Fluids 12 (7) (2000) 1843–1863.
[49] M. Colket, J. Heyne, M. Rumizen, J.T. Edwards, M. Gupta, W.M. Roquemore, J.P. Moder, J.M. Tishkoff, C. Li, An overview of the national jet fuels combustion program, 54th AIAA Aerospace Sciences Meeting, AIAA-paper 0177 (2016).
[50] J.T. Edwards, Reference jet fuels for combustion testing, 55th AIAA Aerospace Sciences Meeting (2017), p. 0146.
[51] H. Wang, X. You, A.V. Joshi, S.G. Davis, A. Laskin, F. Egolfopoulos, C.K. Law, USC Mech Version II. high-temperature combustion reaction model of H2/CO/C1-C4 compounds, http://ignis.usc.edu/USC_Mech_II.htm(2007).
[52] C.P. Fenimore, Formation of nitric oxide in premixed hydrocarbon flames, Symp. (Int.) Combust. 13 (1971) 373–380.
[53] J. Luche, Obtention de modeles cinétiques réduits de combustion. Application à un mécanisme du kérosène, Université d'Orléans, 2003 Ph.d. thesis.
[54] J. Cai, S.-M. Jeng, R. Tacina, The structure of a swirl-stabilized reacting spray issued from an axial swirler, 43rd AIAA Aerospace Sciences Meeting and Exhibit (2005).
[55] T. Turányi, Reduction of large reaction mechanisms, New J. Chem. 14 (1990) 795–803.
[56] P. Pepiot-Desjardins, H. Pitsch, An efficient error propagation based reduction method for large chemical kinetic mechanisms, Combust. Flame 154 (1) (2008) 67–81.
[57] T. Lovas, P. Amnéus, F. Mauss, E. Mastorakos, Comparison of automatic reduction procedures for ignition chemistry, Proc. Combust. Inst. 29 (1) (2002) 1387–1393.
[58] P. Pepiot, Automatic Strategies to Model Transportation Fuel Surrogates, Stanford University, 2008 Ph.d. thesis.
[59] D.G. Goodwin, H.K. Moffat, R.L. Speth, Cantera: an object-oriented software toolkit for chemical kinetics, thermodynamics, and transport processes, 2017, (http://www.cantera.org). Version 2.1.1.
[60] H. Pitsch, FlameMaster: a C++ computer program for 0D combustion and 1D laminarflame calculations (1996). https://web.stanford.edu/group/pitsch/FlameMaster.htm
[61] Y. Fu, S.-M. Jeng, R. Tacina, Characteristics of the swirling flow generated by an axial swirler, ASME Turbo Expo 2005: Power for Land, Sea, and Air, American Society of Mechanical Engineers (2005), pp. 517–526.
[62] A. Iannetti, N.-S. Liu, F. Davoudzadeh, The Effect of Spray Initial Conditions on Heat Release and Emissions in LDI CFD Calculations, NASA Report No. NASA/TM—2008-214522, NASA Glenn Research Center, Cleveland, OH, 2008.
[63] R. Lecourt, G. Linassier, G. Lavergne, Detailed characterisation of a swirled air/kerosene spray in reactive and non-reactive conditions downstream from an actual turbojet injection system, ASME Turbo Expo: Turbine Technical Conference and Exposition, American Society of Mechanical Engineers (2011), pp. 185–194.
[64] J. Apeloig, F.-X. d'Herbigny, F. Simon, P. Gajan, M. Orain, S. Roux, Liquid-fuel behavior in an aeronautical injector submitted to thermoacoustic instabilities, J. Propuls. Power 31 (1) (2014) 309–319.
[65] H. El-Asrag, A. Iannetti, S. Apte, Large eddy simulations for radiation-spray coupling for a lean direct injector combustor, Combust. Flame 161 (2) (2014) 510–524.
[66] S. Honnet, K. Seshadri, U. Niemann, N. Peters, A surrogate fuel for kerosene, Proc. Combust. Inst. 32 (1) (2009) 485–492.
[67] M. Maxey, J. Riley, Equation of motion for a small rigid sphere in a nonuniform flow, Phys. Fluids 26 (4) (1983) 883–889.
[68] L. Schiller, Z. Naumann, A drag coefficient correlation, Z. Ver. Deutsch. Ing 77 (1) (1935) 318–320.
[69] W. Ranz, W. Marshall, Evaporation from drops, Chem. Eng. Prog. 48 (3) (1952) 141–146.
[70] G. Hubbard, V. Denny, A. Mills, Droplet evaporation: effects of transients and variable properties, Int. J. Heat Mass Transf. 18 (9) (1975) 1003–1008.
[71] B. Abramzon, W. Sirignano, Droplet vaporization model for spray combustion calculations, Int. J. Heat Mass Transf. 32 (9) (1989) 1605–1618.
[72] F. Nicoud, H. Baya Toda, O. Cabrit, S. Bose, J. Lee, Using singular values to build a subgrid-scale model for Large Eddy Simulations, Phys. Fluids 23 (8) (2011) 085106.
[73] D. Paulhiac, Modélisation de la combustion d'un spray dans un brûleur aéronautique, CERFACS, 2015 Ph.d. thesis.

[74] F. Charlette, D. Veynante, C. Meneveau, A power-law wrinkling model for LES of premixed turbulent combustion: Part I - Non-dynamic formulation and initial tests, Combust. Flame 131 (1) (2002) 159–180.
[75] P. Fede, O. Simonin, P. Villedieu, K.D. Squires, Stochastic modeling of the turbulent subgrid fluid velocity along inertial particle trajectories, Summer Program, Center for Turbulence Research, Stanford University (2006), pp. 247–258.
[76] CERFACS, LES solver AVBP 7.0, 2017, (http://www.cerfacs.fr/avbp7x/index.php).
[77] O. Colin, M. Rudgyard, Development of High-Order Taylor-Galerkin schemes for LES, J. Comput. Phys. 162 (2) (2000) 338–371.
[78] T. Poinsot, S.K. Lele, Boundary conditions for direct simulations of compressible viscous flows, J. Comput. Phys. 101 (1) (1992) 104–129.
[79] M. Sanjosé, J.M. Senoner, F. Jaegle, B. Cuenot, S. Moreau, T. Poinsot, Fuel injection model for Euler–Euler and Euler–Lagrange large-eddy simulations of an evaporating spray inside an aeronautical combustor, Int. J. Multiph. Flow 37 (5) (2011) 514–529.
[80] N. Iafrate, Simulation aux grandes echelles diphasique dans les moteurs downsizés à allumage commandé, IFPEN, 2016 Ph.d. thesis.
[81] R. Bilger, The structure of turbulent nonpremixed flames, Symp. (Int.) Combust. 22 (1) (1989) 475–488.
[82] H. Yamashita, M. Shimada, T. Takeno, A numerical study on flame stability at the transition point of jet diffusion flames, Symp. (Int.) Combust. 26 (1) (1996) 27–34.
[83] A. Neophytou, E. Mastorakos, R.S. Cant, The internal structure of igniting turbulent sprays as revealed by complex chemistry DNS, Combust. Flame 159 (2) (2012) 641–664.
[84] X. Mercier, M. Orain, F. Grisch, Investigation of droplet combustion in strained counterflow diffusion flames using planar laser-induced fluorescence, Appl. Phys. B Lasers Optics 88 (1) (2007) 151–160.
[85] S.M. Correa, A review of NOX formation under gas-turbine combustion conditions, Combust. Sci. Technol. 87 (1-6) (1993) 329–362.
[86] J.A. Miller, C.T. Bowman, Mechanism and modeling of nitrogen chemistry in combustion, Prog. Energy Combust. Sci. 15 (4) (1989) 287–338.
[87] J.W. Bozzelli, A.M. Dean, O + NNH: A possible new route for NOx formation in flames, Int. J. Chem. Kinet. 27 (11) (1995) 1097–1109.